This is a repository copy of *Mapping the core of the Tarantula Nebula with VLT-MUSE – III. A template for metal-poor starburst regions in the visual and far-ultraviolet*.

White Rose Research Online URL for this paper:
https://eprints.whiterose.ac.uk/209298/

Version: Published Version

Article:

Crowther, P.A. orcid.org/0000-0001-6000-6920 and Castro, N. orcid.org/0000-0003-0521-473X (2024) Mapping the core of the Tarantula Nebula with VLT-MUSE – III. A template for metal-poor starburst regions in the visual and far-ultraviolet. Monthly Notices of the Royal Astronomical Society, 527 (3). pp. 9023-9047. ISSN 0035-8711

https://doi.org/10.1093/mnras/stad3698

Reuse

This article is distributed under the terms of the Creative Commons Attribution (CC BY) licence. This licence allows you to distribute, remix, tweak, and build upon the work, even commercially, as long as you credit the authors for the original work. More information and the full terms of the licence here: https://creativecommons.org/licenses/

Takedown

If you consider content in White Rose Research Online to be in breach of UK law, please notify us by emailing eprints@whiterose.ac.uk including the URL of the record and the reason for the withdrawal request.

eprints@whiterose.ac.uk
https://eprints.whiterose.ac.uk/

Monthly Notices of the ROYAL ASTRONOMICAL SOCIETY

MNRAS **527,** 9023–9047 (2024) https://doi.org/10.1093/mnras/stad3698
Advance Access publication 2023 November 29

Mapping the core of the Tarantula Nebula with VLT-MUSE – III. A template for metal-poor starburst regions in the visual and far-ultraviolet

Paul A. Crowther [1]★ and N. Castro [2]

[1] *Department of Physics and Astronomy, University of Sheffield, Sheffield, S3 7RH, UK*
[2] *Leibniz-Institut für Astrophysik Potsdam, An der Sternwarte 16, D-14482 Potsdam, Germany*

Accepted 2023 November 24. Received 2023 November 24; in original form 2023 September 19

ABSTRACT

We present the integrated VLT-MUSE spectrum of the central 2 × 2 arcmin^2 (30 × 30 pc^2) of NGC 2070, the dominant giant H II region of the Tarantula Nebula in the Large Magellanic Cloud, together with an empirical far-ultraviolet spectrum constructed via LMC template stars from the ULLYSES survey and Hubble Tarantula Treasury Project UV photometry. NGC 2070 provides a unique opportunity to compare results from individual stellar populations (e.g. VLT FLAMES Tarantula Survey) in a metal-poor starburst region to the integrated results from the population synthesis tools Starburst99, Charlot & Bruzual, and BPASS. The metallicity of NGC 2070 inferred from standard nebular strong line calibrations is ∼0.4 ± 0.1 dex lower than obtained from direct methods. The Hα inferred age of 4.2 Myr from Starburst99 is close to the median age of OB stars within the region, although individual stars span a broad range of 1–7 Myr. The inferred stellar mass is close to that obtained for the rich star cluster R136 within NGC 2070, although this contributes only 21 per cent to the integrated far-UV continuum. He II λ1640 emission is dominated by classical WR stars and main sequence WNh + Of/WN stars. Around 18 per cent of the NGC 2070 far UV continuum flux arises from very massive stars with ≥100 M$_\odot$, including several very luminous Of supergiants. None of the predicted population synthesis models at low metallicities are able to successfully reproduce the far-UV spectrum of NGC 2070. We attribute issues to the treatment of mass-loss in very massive stars, the lack of contemporary empirical metal-poor templates, plus WR stars produced via binary evolution.

Key words: galaxies: clusters: individual: R136 – stars: massive - galaxies: Magellanic Clouds – ISM: HII regions: ultraviolet: stars – galaxies: starburst.

1 INTRODUCTION

The Tarantula Nebula (30 Doradus) in the Large Magellanic Cloud (LMC) is intrinsically the brightest star-forming region within the Local Group of galaxies (Crowther 2019). It has been the subject of numerous studies across the electromagnetic spectrum (Vacca et al. 1995; Sabbi et al. 2013; Crowther et al. 2022; Wong et al. 2022; Fahrion & De Marchi 2023). Its low (half-solar) metallicity and high star formation intensity are more typical of knots star-forming galaxies at z ∼2–3 (Steidel et al. 2016; Johnson et al. 2017) than local systems, owing to its very rich stellar content (Schneider et al. 2018a). Indeed, 30 Doradus has nebular conditions that are reminiscent of Green Pea galaxies (Cardamone et al. 2009), which are local extreme emission-line galaxies, some of which are known to be Lyman continuum leakers (Micheva et al. 2017).

The Tarantula Nebula is host to hundreds of massive stars, including very massive stars (VMS) located in the central, dense star cluster R136 (Massey & Hunter 1998; Crowther et al. 2010) and the extended giant H II region NGC 2070, the central ionized nebula within the Tarantula (Bestenlehner et al. 2014). Its proximity permits observation and analysis of individual massive OB and Wolf-Rayet stars (Melnick 1985; Selman et al. 1999; Evans et al. 2011). Star formation in the Tarantula Nebula began at least 15–30 Myr ago, as witnessed by the Hodge 301 cluster, with an upturn in its rate of star formation in the last 5–10 Myr (Schneider et al. 2018b). Star formation is still ongoing, as witnessed by clumps of molecular gas observed with the Atacama Large Millimeter Array (Wong et al. 2022).

The proximity of the LMC provides a unique opportunity to study a rich, intensively star-forming region individually, via its resolved stellar content (Doran et al. 2013), and collectively, via its integrated light via application of population synthesis models. If the LMC were located at a distance of 10 Mpc, R136, NGC 2070, and the Tarantula would subtend diameters of 0.04, 0.8, and 6 arcsec, respectively (Crowther 2019). Population synthesis models are widely employed to interpret far-ultraviolet (UV) spectroscopy of unresolved star clusters at Mpc distances (Chandar, Leitherer & Tremonti 2004; James et al. 2014; Sirressi et al. 2022), local star-forming galaxies (Wofford, Leitherer & Salzer 2013; Berg et al. 2022) plus those at z > 2 observed with large ground-based telescopes (Steidel et al. 2016; Saxena et al. 2020) or *James Webb Space Telescope* (Carnall et al. 2023; Curtis-Lake et al. 2023).

Although the nebular properties of the entire 30 Doradus region has previously been studied (Kennicutt et al. 1995; Pellegrini, Baldwin &

★ E-mail: Paul.crowther@sheffield.ac.uk

© 2023 The Author(s).
Published by Oxford University Press on behalf of Royal Astronomical Society. This is an Open Access article distributed under the terms of the Creative Commons Attribution License (http://creativecommons.org/licenses/by/4.0/), which permits unrestricted reuse, distribution, and reproduction in any medium, provided the original work is properly cited.

Downloaded from https://academic.oup.com/mnras/article/527/3/9023/7455889 by guest on 16 February 2024

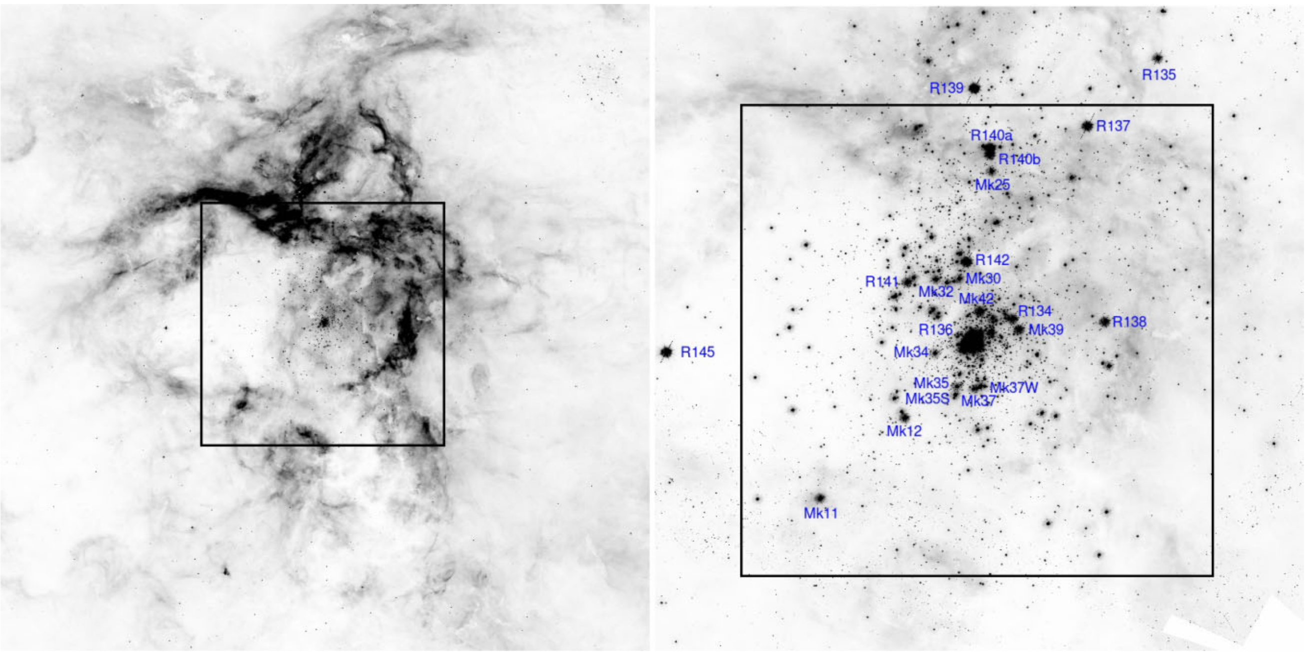

Figure 1. Left-hand panel: HST ACS/F658N image of the central region of 30 Doradus (320 × 320 arcsec^2) from HTTP (Sabbi et al. 2013) including MUSE field of view (black box). North is up, East to the left. Hodge 301 can be seen to the upper right. Right-hand panel: HST WFC3/F336W image of central region of NGC 2070 (165 × 165 arcsec^2) from HTTP, with selected bright sources labelled. The white region to the lower right is not included in the F336W footprint.

Ferland 2010), here we focus on the central region of NGC 2070 observed with the Multi-unit Spectroscopic Explorer (MUSE) mounted at the Very Large Telescope (VLT), as part of its original Science Verification programme. Castro et al. (2018) introduce the data set and provide a stellar census and nebular kinematic properties, while Castro et al. (2021b) present a spectroscopic analysis of OB stars. This region is host to the central R136 star cluster, several WR stars, including the R140 complex, plus several cool supergiants such as Melnick 9.

Age estimates of OB stars within NGC 2070 (external to R136) range from 1 to 7 Myr, with a median age of 3.6 Myr (Schneider et al. 2018b). To date, only the central cluster R136 has been observed in the far-UV, both collectively (Heap, Ebbets & Malumuth 1992) and individually (Crowther et al. 2016), the latter obtaining a cluster age of ∼1.5 Myr (see also Brands et al. 2022). Several other luminous early-type stars within NGC 2070 have been observed in the far-UV with COS or STIS instruments aboard *Hubble Space Telescope (HST)*, plus a large sample of far-UV template spectra of LMC OB stars have been obtained via the *HST* initiative ULLYSES (Roman-Duval et al. 2020; Crowther 2022). Consequently, we are able to construct an empirical integrated spectrum of the MUSE field of-view in the far-UV, for comparison with predictions from (theoretical) population synthesis models Starburst99 (Leitherer et al. 1999, 2014), Charlot & Bruzual (Bruzual & Charlot 2003; Plat et al. 2019), and BPASS (Eldridge et al. 2017; Stanway & Eldridge 2018).

The present study completes the analysis of NGC 2070 MUSE Wide Field Mode (WFM) observations and is structured as follows. We provide a brief summary of visual MUSE observations of NGC 2070 and describe how the far-UV spectrum of NGC 2070 is constructed in Section 2. The integrated MUSE data set is analysed in Section 3, with an emphasis on nebular properties and optical Wolf-Rayet bumps, with the far-UV spectrum compared to predictions from various population synthesis models in Section 4. A comparison between individual and cumulative results is provided in Section 5, together with brief conclusions. Initial results for nebular, stellar, and integrated properties of the MUSE WFM data sets were presented in Crowther et al. (2017).

2 NGC 2070 SPECTROSCOPIC DATA SETS

2.1 Visual observations

MUSE is a wide-field, integral-field spectrograph providing intermediate resolution (R ∼2000) spectroscopy from 4600 to 9350 Å (Bacon et al. 2010). Four overlapping MUSE WFM pointings were obtained at the VLT in August 2014 via a Science Verification programme (PI: J. Melnick), providing a 2 × 2 arcmin^2 (30 × 30 pc^2) mosaic which encompasses both the R136 star cluster and R140, an aggregate of WR stars to the north (Castro et al. 2018). The MUSE field of view is indicated on Hubble Tarantula Treasury Project[1] (HTTP; Sabbi et al. 2013). About 320 × 320 arcsec^2 ACS/F658N and 165 × 165 arcsec^2 WFC3/F336W images in Fig. 1 in which selected bright sources are identified in the latter. A larger footprint, especially to the north, would be required to fully sample the bright nebulosity of NGC 2070, but MUSE field of view includes ∼50 per cent of the far-UV continuum of the entire Tarantula.[2]

The MUSE spatial resolution spanned 0.7–1.1 arcsec, corresponding to a mean spatial resolution of 0.22 ± 0.04 pc. Four exposures of 600 s for each pointing provided a continuum S/N exceeding 50 for 600 sources in the yellow. The integrated MUSE green-red spectrum of NGC 2070 is presented in Fig. 2, with nebular properties

[1] https://archive.stsci.edu/hlsp/http

[2] We have followed the approach set out in Section 2.2 to estimate $F_{1500} \sim 1.2 \times 10^{-11}$ erg s^{-1} cm^{-2} Å^{-1} for the region of the Tarantula exterior to the MUSE footprint

Downloaded from https://academic.oup.com/mnras/article/527/3/9023/7455889 by guest on 16 February 2024

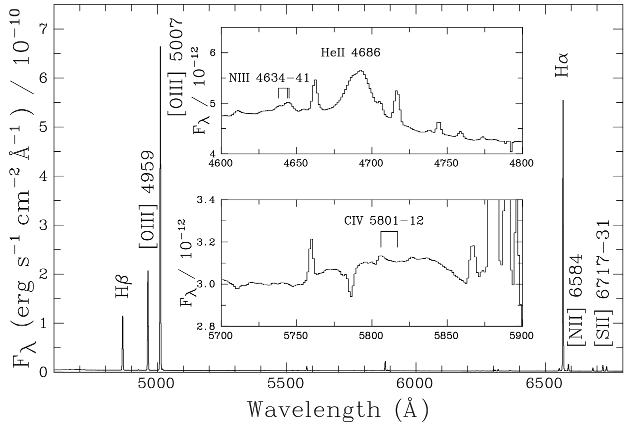

Figure 2. Integrated MUSE spectrum of NGC 2070, updated from Crowther et al. (2017), revealing a striking emission line spectrum, with nebular properties (e.g. high [O III] λ5007/Hβ, low [N II] λ6584/Hα) reminiscent of Green Pea galaxies (Cardamone et al. 2009). WR bumps are observed in the blue (upper inset, He IIλ4686 arising from primarily WN stars) and yellow (lower inset, C IV $\lambda\lambda$5801-12 due to WC stars). Nebular lines in the insets include [Fe III] λ4658, [Ar IV] λ4711, [N II] λ5755, and He I λ5876.

reminiscent of Green Pea galaxies (Cardamone et al. 2009), plus WR bumps in the blue (upper inset), and red (lower inset). Recent MUSE Narrow Field Mode observations of the R136 cluster are presented in Castro et al. (2021a).

2.2 Far-ultraviolet observations

The combination of VLT/MUSE (Castro et al. 2018), VLT/FLAMES (Evans et al. 2011), and *HST*/STIS (Crowther et al. 2016) spectroscopy provide near complete spectral type census of bright early-type stars in the Tarantula (Schneider et al. 2018a; Crowther 2019). This census permits us to construct an integrated far-UV spectrum of the region within the MUSE mosaic discussed in Section 2.1, by combining empirical data sets for a subset of stars (those with far-UV spectroscopy) with suitable templates for the remainder (those lacking far-UV spectroscopy at $R \geq 2000$). Empirical *HST* COS or STIS spectroscopy is available for a subset of individual UV-bright sources, which are rebinned to R ∼2000. These are supplemented by Goddard High Resolution Spectroscopy (GHRS) G140L observations of the central 2 × 2 arcsec^2 R136a cluster (Heap, Ebbets & Malumuth 1992), also obtained at R ∼2000.[3] The cumulative far-UV spectrum was constructed used the Starlink spectroscopic package DIPSO (Howarth et al. 2004).

For the majority of sources, far-UV spectroscopy of LMC OB and WR templates from ULLYSES[4] (Roman-Duval et al. 2020) are utilized (up to DR6), supplemented by COS and STIS data sets from GO programmes (GO 15629, Mahy; GO 16272, Shenar). Templates are anchored to estimates of 1500 Å fluxes determined from F275W or F336W photometry from HTTP (Sabbi et al. 2016). Since HTTP photometry of 30 Doradus is incomplete, we also utilize WFC3/F336W photometry from De Marchi et al. (2011) or WFPC2/F336W photometry from Hunter et al. (1995). We provide details of templates in Tables A1 and A2. Gaps in spectra arise from incomplete spectral coverage of templates (e.g. COS G130M + G160M).

[3]The spectral resolution of STIS/G140L observations from Crowther et al. (2016) achieved R ∼1000, too low for our purposes here
[4]https://ullyses.stsci.edu/

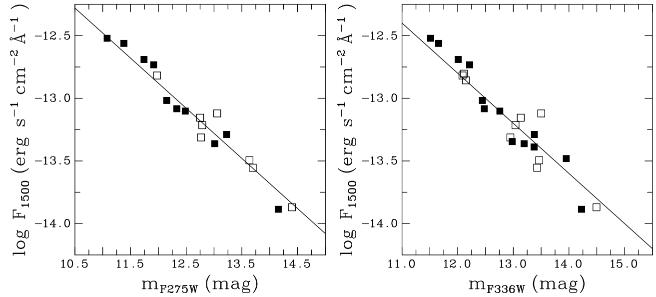

Figure 3. Relationship between $m_{\rm F275W}$ (left) or $m_{\rm F336W}$ (right) and far-UV flux, F_{1500}, for O stars in 30 Doradus (solid within MUSE field) with far-UV spectroscopy and HST/WFC3 photometry (Sabbi et al. 2013). The solid line is a linear fit to all observations.

We estimate λ1500 fluxes of O and WR stars lacking far-UV spectroscopy from a calibration of F275W photometry anchored by O stars within 30 Doradus for which far-UV spectroscopy is available, as shown in the left-hand panel of Fig. 3, whose linear fit is

$$\log F_{1500} = -0.4(m_{\rm F275W} + 20.20 \pm 0.08) \qquad (1)$$

F275W photometry is not available throughout the MUSE field of view, whereas F336W is available for all sources, for which a calibration is presented in the right-hand panel of Fig. 3, and a linear fit is

$$\log F_{1500} = -0.4(m_{\rm F336W} + 20.00 \pm 0.15). \qquad (2)$$

Fluxes for individual stars in 30 Doradus used in the calibration are provided in Appendix C (Table C1). For B supergiants, λ1500 fluxes are reduced by a scale factor of 0.85 (B0.5 ± 0.5), 0.65 (B1–3), or 0.5 (B4–9) from a comparison between spherical non-LTE model atmospheres of far- to near-UV fluxes of O and B stars (Hillier & Miller 1998). For B dwarfs, λ1500 fluxes are reduced by a factor of 0.77 (B0.5 ± 0.5) or 0.65 (B1.5 ± 0.5) from a comparison between TLUSTY plane parallel non-LTE model atmospheres of O and B stars (Lanz & Hubeny 2007). We also adjust the $\lambda\lambda$1160–1700 slopes of templates according to their $m_{\rm F336W} - m_{\rm F555W}$ colours as discussed in Appendix C

We incorporate a total of 227 sources with spectral types and estimated fluxes $F_{1500} \geq 10^{-14}$ erg s^{-1} cm^{-2}Å^{-1} into our cumulative far-UV spectrum, which are listed in Table B1. Of these, 29 lie within the R136a 2 × 2 arcsec^2 GHRS footprint, 13 possess HST COS (G130M + G160M or G140L) or STIS (E140M) spectroscopy, such that the remaining 185 require ULLYSES templates, several of which have known far-UV fluxes courtesy of HST/STIS G140L spectroscopy (Massey et al. 2005). Although R136a stars exterior to the GHRS footprint have been observed in the far-UV with HST/STIS G140L (Crowther et al. 2016), their slit loss corrections are uncertain, such that F_{1500} from GHRS is ∼20 per cent higher than the sum of individual fluxes. Consequently, we adopt F_{1500} from calibrations for stars exterior to the GHRS aperture in common with (Crowther et al. 2016).

HSH95 17, alias #9 from Kalari et al. (2022), is included in Table B1 despite an uncertain spectral type since it lies within the GHRS 2 × 2 arcsec^2 footprint such that we do not require a bespoke UV template. Several other sources that would qualify on the basis of their far-UV fluxes are excluded due to unknown spectral types (e.g. HSH95 76, HSH95 87, and SMB 136), which is

Downloaded from https://academic.oup.com/mnras/article/527/3/9023/7455889 by guest on 16 February 2024

Table 1. Summary of sources brighter than $F_{1500} = 10^{-14}$ erg s^{-1} cm^{-2}Å^{-1} contributing to the far-UV continuum of the MUSE pointing, broken down by subtype (primary in binaries) and whether empirical UV spectroscopy or templates were utilized. The R136a GHRS spectrum comprises 3 WNh stars and 26 O stars [assuming HSH95-17 is an O star, Kalari et al. (2022)], each contributing ∼40 per cent and 60 per cent of the far-UV flux of R136a. 20 sources are confirmed spectroscopic binaries, comprising 15 systems with an O-type primary, 3 with an Of/WN or WN5h primary, plus 1 each with a Wolf-Rayet or B-type primary. 180 additional faint sources with $5 \times 10^{-16} \leq F_{1500} < 1.0 \times 10^{-14}$ erg s^{-1} cm^{-2}Å^{-1} are incorporated via a B0 V template scaled to the sum of their far-UV fluxes.

Subtype	Empirical		Template		Total	
	N	F_{1500}	N	F_{1500}	N	F_{1500}
O	34	1.92×10^{-12}	159	7.44×10^{-12}	193	9.36×10^{-12}
Of/WN + WNh	7	1.31×10^{-12}	5	0.46×10^{-12}	12	1.77×10^{-12}
B	0	···	16	1.40×10^{-12}	16	1.40×10^{-12}
Wolf-Rayet	1	0.39×10^{-12}	5	0.67×10^{-12}	6	1.06×10^{-12}
Sum	42	3.62×10^{-12}	185	9.97×10^{-12}	227	13.59×10^{-12}
Sum + Faint	···	···	180	0.83×10^{-12}	407	14.42×10^{-12}

necessary to incorporate suitable UV templates. Their contribution to the cumulative far-UV flux is negligible (∼1 per cent).

Twenty sources in Table B1 are confirmed spectroscopic binaries, although not all stars have been subject to spectroscopic monitoring, so the true binary frequency will be significantly higher. Confirmed multiple systems among the UV-brightest sources ($F_{1500} \geq 5 \times 10^{-14}$ erg s^{-1} cm^{-2}Å^{-1}) include O-type binaries HSH95 39, HSH95 42 within R136a (Massey, Penny & Vukovich 2002), Wolf-Rayet and O-type binaries R140b, c and d (Shenar et al. 2019; Walborn et al. 2014), plus colliding wind binaries R136c, Mk 33Na, Mk 34, and Mk 39 (Crowther et al. 2022).

The cumulative far-UV flux of the individual 227 sources is 1.36×10^{-11} erg s^{-1} cm^{-2}Å^{-1}. An additional 180 sources with known spectral types possess far-UV fluxes in the range $5 \times 10^{-16} \leq F_{1500} < 1.0 \times 10^{-14}$ erg s^{-1} cm^{-2}Å^{-1}. We account for these collectively via a B0 V template scaled to their cumulative far-UV flux (8.35×10^{-13} erg s^{-1} cm^{-2}Å^{-1}), such that they contributes an additional ∼6 per cent to the total far-UV continuum. Table 1 provides a spectral subtype of the sources contributing to the far-UV continuum. Stars possessing empirical far-UV spectroscopy contribute 25 per cent of the total. The dominant contribution arises from large numbers of O stars (65 per cent), although modest populations of very massive main-sequence WN (WNh) and transition Of/WN stars (12 per cent), B stars, primarily supergiants (10 per cent), and classical WR stars (7 per cent) also make non-negligible contributions.

Fig. 4 presents the cumulative far-UV spectrum of the MUSE field, including contributions from OB-type (pink), classical WR (blue) stars plus main sequence WNh and Of/WN stars (red). We have split relative contributions from O and WNh stars to the core of R136a by adjusting their combined HST STIS/G140L spectra from (Crowther et al. 2016) to the flux of the HST/GHRS spectrum. He II λ1640 is unusually strong ($W_\lambda = 4.7 \pm 0.2$ Å) and broad full-width half maximum (FWHM = 9.3 ± 0.3 Å). Figs A1–A4 illustrate the contribution of empirical data sets and templates to the far-UV spectra of individual spectral types. All subtypes contribute to the strong C IV λ1550 P Cygni profile, although it is apparent that He II λ1640 emission is dominated by classical WR stars (56 per cent) plus WNh and Of/WN stars (31 per cent). All subtypes contribute to N V λ1240, aside from B supergiants, although B supergiants and classical WR stars are the primary contributors to P Cygni Si IV λ1400.

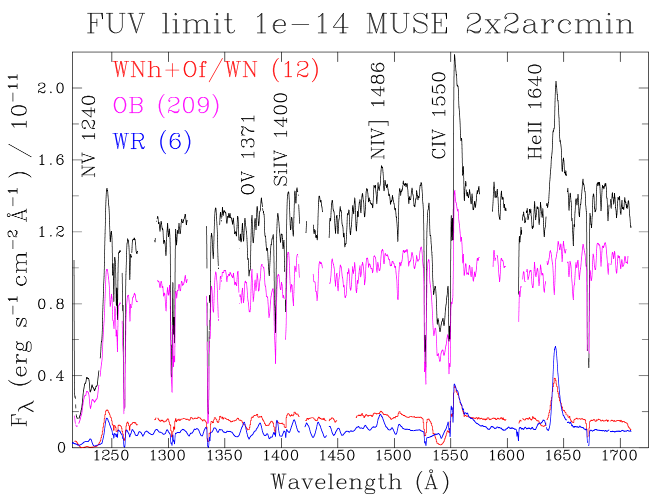

Figure 4. Cumulative far-UV spectrum of the central region of NGC 2070 (black) inferred from a combination of empirical (42 stars, 25 per cent of total), LMC templates (185 stars, 69 per cent of total) plus faint OB stars (180 stars, 6 per cent of total), highlighting contributions from OB stars (pink), Of/WN and WNh stars (red), and classical WR stars (blue). He II λ1640 emission is dominated by classical WR stars (56 per cent) and very massive main sequence stars (31 per cent), with the remainder arising from Of supergiants (e.g. Mk 42, R136a5). Gaps in spectra arise from incomplete spectral coverage of templates (e.g. COS G130M + G160M).

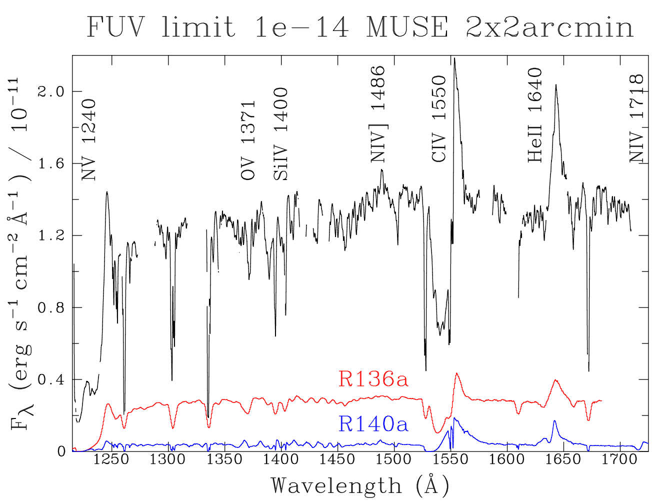

Figure 5. Cumulative far-UV spectrum of the central region of NGC 2070 (black) together with the integrated STIS/G140L spectrum of the R136a cluster (red, 3.6 × 3.6 arcsec^2) from Crowther et al. (2016) plus STIS/E140M spectrum of R140a (blue), the UV brightest source in the MUSE field, which is host to classical WN+WC stars. Gaps in spectra arise from incomplete spectral coverage of templates (e.g. COS G130M + G160M).

In Table B1, we have flagged ∼18 VMS with initial masses in excess of ∼100 M$_\odot$ on the basis of spectroscopic results (Bestenlehner et al. 2014; Tehrani et al. 2019; Brands et al. 2022). The majority of these have WN5h, Of/WN or O2–4 If spectral types, exceptions include R136a7 (O3 III(f*)), R136a4 (O3 V), and VFTS 506 (ON2 V). In spite of their scarcity, 18 per cent of the NGC 2070 far-UV flux arises from VMS.

Fig. 5 compares the cumulative far-UV spectrum to the integrated STIS/G140L spectrum of R136a from Crowther et al. (2016), contributing 22 per cent of the far-UV continuum flux, plus the

Downloaded from https://academic.oup.com/mnras/article/527/3/9023/7455889 by guest on 16 February 2024

Table 2. Primary contributors to the integrated He II λ1640 emission line (F_{1640} units of 10^{-12} erg s^{-1} cm^{-2}) in the central 30 × 30 pc^2 region of NGC 2070, including the cumulative line flux from the central cluster R136a which is dominated by WN5h stars R136a1, a2 and a3 (Crowther et al. 2016). Details of templates are provided in Table A2.

Source	Sp Type	F_{1640}	Obs	VMS
R136a	3×WN5h+O4 If/WN8 + ..	13.	STIS/G140L	8✓
R140a	WC4+WN6 + ..	12.	STIS/E140M	···
R140b	WN5(h) + O	9.	WN6 template	···
R134	WN6(h)	6.5	WN6 template	···
Mk 53	WN8(h)	2.2	WN7 template	···
Mk 49	WN6(h)	2.1	WN6 template	···
Mk 33Sb	WC5	2.1	WC4 template	···
R136c	WN5h +	1.8	WN5h template	✓
Mk 34	WN5h + WN5h	1.6	WN5h template	2✓
Mk 39	O2.5 If/WN6 +	1.1	COS/G130M + G160M	✓
Mk 42	O2 If*	0.8	STIS/E140M	✓
Mk 35	O2 If/WN5	0.8	O2If/WN5 template	✓
Mk 37a	O3.5 If/WN7	0.5	O3.5 If/WN7 template	✓
Total		57.	···	···

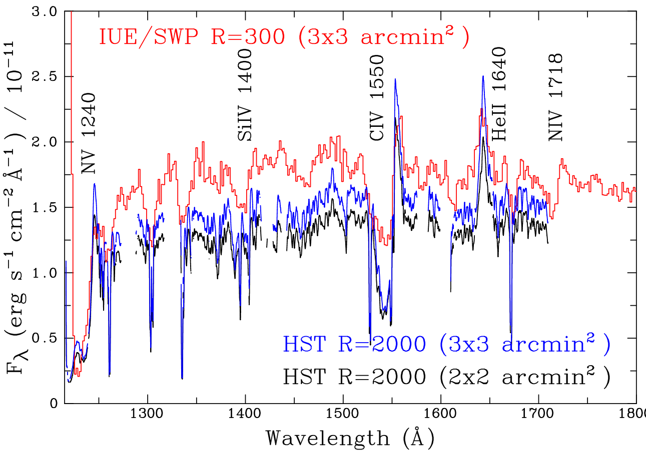

Figure 6. Integrated *IUE*/SWP spectra of the central 3 × 3 arcmin^2 (red) region of NGC 2070 from Vacca et al. (1995) together with our cumulative far-UV spectrum for the central 2 × 2 arcmin^2 (black) and 3 × 3 arcmin^2 (blue) regions. N IV λ1718 is prominent in the large aperture *IUE* data set despite its low ($R \sim 300$) spectral resolution. *IUE* observations suggest 15 per cent higher far-UV flux levels owing to a combination of flux calibration differences or unresolved stars (primarily B-type) omitted from our study.

STIS/E140M spectrum of R140a (VFTS 507), the brightest individual source in the MUSE field (3 per cent of far-UV continuum flux), host to classical WN + WC stars. Neither of the WR stars within R140a are known to be binaries (Bartzakos, Moffat & Niemela 2001; Shenar et al. 2019), although the complete stellar content of R140a remains uncertain. R136a possesses an extremely strong He II λ1640 emission with respect to typical young star clusters, but the richness of the surrounding massive star population in NGC 2070 is such that it only contributes a quarter of the integrated emission line flux of He II λ1640. Table 2 lists the primary contributors to F_{1640}, the majority of which originates from classical WR stars, notably R140a.

Vacca et al. (1995) have previously scanned NGC 2070 with *IUE* with the short wavelength camera (SWP), at low spectral resolution ($R \sim 300$) using the large 10 × 20 arcsec^2 aperture, providing integrated spectra for the central 20 × 20 arcsec^2, 1 × 1 arcmin^2, and 3 × 3 arcmin^2 regions. Fig. 6 compares the integrated spectrum of the central 3 × 3 arcmin^2 region (red) with our cumulative far-UV spectrum of the 2 × 2 arcmin^2 MUSE region (black). The overall shape of the spectra are similar, but the continuum flux of our far-UV spectrum is only ∼80 per cent of the large *IUE* aperture. N IV λ1718 is prominent in the large aperture *IUE* data set despite its low spectral resolution.

Table B2 lists additional stars with known spectral types brighter than 1.0×10^{-14} erg s^{-1} cm^{-2} Å^{-1} within the large 3 × 3 arcmin^2 *IUE* aperture. These increase the far-UV continuum flux by 1.7×10^{-12} erg s^{-1} cm^{-2} Å^{-1}, the majority of which is supplied by R135, R139, and R145. Owing to their relative isolation (Fig. 1), far-UV flux levels for these three bright stars are drawn from low-resolution *IUE*/SWP large aperture spectroscopy (Fitzpatrick & Savage 1984).

The blue spectrum in Fig. 6 additionally incorporates all stars listed in Table B2, and reveals a difference of ∼15 per cent in global far-UV flux levels between *IUE* and our approach using *HST* observations. The difference likely arises from the combination of absolute flux calibration and the omission of a diffuse far-UV background from unresolved stars in our study – recall 20 per cent of the integrated far-UV continuum of the rich R136 cluster was from an intra-cluster background (Crowther et al. 2016). Collectively, B-type main sequence stars – lacking strong UV wind features – will dominate this population.

3 ANALYSIS OF INTEGRATED VISUAL SPECTROSCOPY

3.1 Nebular properties

As shown in Fig. 2, the integrated MUSE spectrum of NGC 2070 is dominated by nebular emission lines, plus broad, weak Wolf-Rayet features. Here we undertake an analysis of the nebular spectrum with a focus on the inferred metallicity and age/mass of the ionizing stellar population using commonly used spectral synthesis tools Starburst99 (version 7.0.1; Leitherer et al. 1999, 2014), Charlot & Bruzual (Bruzual & Charlot 2003; Plat et al. 2019, hereafter CB19) and BPASS (v.2.2.1, Eldridge et al. 2017; Stanway & Eldridge 2018). A detailed study of the integrated 30 Doradus nebula has been undertaken by Pellegrini, Baldwin & Ferland (2011) while Peimbert (2003) utilize VLT/UVES spectroscopy for a detailed chemical analysis.

Table 3 presents measured MUSE line fluxes, intensities, and luminosities (assuming 50 kpc), the former obtained using the `elf` suite within the Starlink package DIPSO (Howarth et al. 2004). Although 30 Doradus is known to have a non-standard dust extinction (De Marchi & Panagia 2014; Maíz Apellániz et al. 2014; Brands et al. 2023), we shall adopt a standard LMC extinction law with $R_V = 3.1$ (Howarth 1983) for the nebular analysis. We obtain $c(H\beta) = 0.54$ from $I(\mathrm{H}\alpha)/I(\mathrm{H}\beta) = 2.86$ for Case B recombination theory for a standard $N_e = 10^2$ cm^{-3} and $T_e = 10^4$ K – these results are consistent with averages of resolved maps from Castro et al. (2018).

$L(\mathrm{H}\alpha) = 1.37 \times 10^{39}$ erg s^{-1} equates to an ionizing output of 10^{51} ph s^{-1}, corresponding to a star formation rate of 0.005 M$_\odot$ yr^{-1} using standard conversions from Kennicutt (1998). Our MUSE data set of the central region of NGC 2070 (30 × 30 pc^2) lies within the extended 30 Doradus region. Pellegrini, Baldwin & Ferland (2010) have investigated a much larger 140 × 80 pc^2 region and highlighted that 50 per cent of the integrated Hα emission originates from relatively low-surface brightness regions.

We used the `temden` routine in IRAF to determine the nebular density and temperature. We obtain $N_e = 240 \pm 10$ cm^{-3} from the standard [S II] 6717/6731 diagnostic, and $N_e = 310^{+220}_{-250}$ cm^{-3} from the weak [Cl III] 5518/5538 diagnostic. Comparable results are obtained from the [Fe III] 4658/4986 ratio (Keenan et al. 2001). The

Downloaded from https://academic.oup.com/mnras/article/527/3/9023/7455889 by guest on 16 February 2024

Table 3. Fluxes (*F*), intensities (*I*) and luminosities (*L*) of nebular emission lines and Wolf-Rayet (WR) bumps in the integrated MUSE spectrum of the 2 × 2 arcmin central region of NGC 2070. Case B recombination theory is adopted together with a standard LMC extinction law (Howarth 1983) and an adopted LMC distance of 50 kpc.

Line	*F* 10^{-11} erg s^{-1} cm^{-2}	*I* 10^{-10} erg s^{-1} cm^{-2}	*L* 10^{38} erg s^{-1}	Notes
N III 4634-41	0.71 ± 0.05	0.42 ± 0.04	0.13 ± 0.01	WR
[Fe III] 4658	0.31 ± 0.02	0.12 ± 0.01	0.04	
He II 4686	2.78 ± 0.06	1.18 ± 0.03	0.35 ± 0.01	WR
[Ar IV] 4711	0.32 ± 0.02	0.14 ± 0.01	0.04	
[Ar IV] 4740	0.10 ± 0.01	0.04 ± 0.01	0.01	
Hβ	40.0 ± 0.1	15.9 ± 0.1	4.8 ± 0.1	
[O III] 4959	69.7 ± 0.2	26.8 ± 0.1	8.0 ± 0.1	
[Fe III] 4986	0.15 ± 0.01	0.06 ± 0.01	0.02	
[O III] 5007	213 ± 1	80.7 ± 0.4	24.1 ± 0.1	
He II 5412	0.07 ± 0.01	0.02	0.01	WR
[Cl III] 5518	0.22 ± 0.01	0.07 ± 0.01	0.02	
[Cl III] 5538	0.17 ± 0.01	0.06 ± 0.01	0.02	
[N II] 5755	0.06 ± 0.01	0.02	0.01	
C IV 5801–12	1.53 ± 0.08	0.47 ± 0.02	0.14 ± 0.01	WR
He I 5876	6.21 ± 0.02	1.87 ± 0.01	0.56 ± 0.01	
[O I] 6300	0.46 ± 0.02	0.13 ± 0.01	0.04	
[S III] 6312	0.89 ± 0.03	0.24 ± 0.01	0.07 ± 0.01	
[N II] 6548	1.49 ± 0.07	0.39 ± 0.02	0.12 ± 0.01	
Hα	176 ± 1	45.7 ± 0.3	13.7 ± 0.1	
[N II] 6584	4.48 ± 0.20	1.16 ± 0.05	0.35 ± 0.01	
He I 6678	2.10 ± 0.01	0.53 ± 0.01	0.16 ± 0.01	
[S II] 6717	3.74 ± 0.01	0.94 ± 0.01	0.28 ± 0.01	
[S II] 6731	3.12 ± 0.01	0.78 ± 0.01	0.23 ± 0.01	
He I 7065	1.88 ± 0.01	0.44 ± 0.01	0.13 ± 0.01	
[Ar III] 7135	7.33 ± 0.01	1.71 ± 0.01	0.51 ± 0.01	
[S III] 9069	21.3 ± 0.2	3.82 ± 0.04	1.14 ± 0.01	

usual [O III] 4363/5007 temperature diagnostic is not available for MUSE observations at $z = 0$, so we use [N II] 5755/6584 to obtain $T_e = 10,400^{+900}_{-700}$ K and [S III] 6312/9069 to obtain $T_e = 8300^{+70}_{-50}$ K. For reference, Peimbert (2003) obtained $N_e = 415 \pm 35$ cm^{-3} ([S II]) and $T_e = 10\,800 \pm 300$ K ([N II]).

We are unable to determine the oxygen abundance from the use of auroral T_e diagnostics (λ4363 [O III] is not available to MUSE at zero redshift). Instead, we rely on strong line calibrations (Maiolino & Mannucci 2019), which are widely used for extragalactic H II regions for which direct temperature determinations are not feasible. The calibration of the N2 index (–1.59) by Marino et al. (2013) implies 12 + log (*O*/*H*) = 8.01 ± 0.32, versus 7.90 ± 0.16 following Curti et al. (2017). The O3N2 index (+ 2.3) lies beyond the calibrated range of Marino et al. (2013), with 12 + log (*O*/*H*) = 8.10 ± 0.21 obtained from Curti et al. (2017), values typical of the present-day Small Magellanic Cloud (SMC) rather than the LMC (Pagel et al. 1978; Russell & Dopita 1990). Use of the integrated 30 Dor nebular fluxes from Pellegrini, Baldwin & Ferland (2010) provides N2 and O3N2 indices of –1.42 and 2.09, indicating 12 + log (*O*/*H*) = 8.10 ± 0.16 or 8.19 ± 0.21, respectively, following the Curti et al. (2017) calibrations.

Contemporary baseline LMC abundances (Vink et al. 2023, Table 1), including 12 + log (*O*/*H*) = 8.36 correspond to a mass fraction of Z = 0.008, although the directly determined gas phase oxygen abundance within 30 Doradus ranges from 12 + log (*O*/*H*) = 8.26 (Vermeij & van der Hulst 2002) to 8.5 (Peimbert 2003). It is clear that standard strong line calibrations significantly underestimate the true oxygen content of NGC 2070, since these are sensitive to ionization parameter as well as abundance (Kewley & Dopita 2002). Consequently, caution should be used when inferring metallicities of low-redshift star-forming galaxies from diagnostics within the MUSE spectral range (see Easeman et al. 2024). By way of a test, spectral synthesis calculations are made for both Z = 0.008 (well matched to NGC 2070) and Z = 0.002 (significantly lower than NGC 2070, albeit inferred from strong line methods).

3.2 Population synthesis

In order to estimate the age and mass of the starburst region consistent with MUSE observations, we have employed several widely used population synthesis packages. Age estimates from Hα are relatively metallicity insensitive, but WR bumps and UV diagnostics are strongly metallicity-dependent. Starburst99 (v7.0.1, Leitherer et al. 1999, 2014) involves a 1 × 10^5 M$_\odot$ burst of star formation, an initial mass function (IMF) from Kroupa (2008) with an upper mass limit of 120 M$_\odot$. Modern non-rotating and rotating Geneva evolutionary models at Solar (Z = 0.014 Ekström et al. 2012) and SMC (Z = 0.002 Georgy et al. 2013) metallicities are available,[5] with the full range of metallicities for historical models available with either standard (Schaller et al. 1992) or enhanced mass-loss (Meynet et al. 1994).

Starburst99 model atmospheres are obtained from either WM-Basic (O, Pauldrach, Hoffmann & Lennon 2001) or PoWR (WR, Gräfener, Koesterke & Hamann 2002), with ionizing fluxes from Smith, Norris & Crowther (2002) and Leitherer et al. (2010) and empirical UV spectral templates drawn from either the Milky Way or Magellanic Clouds (Robert, Leitherer & Heckman 1993).

Observed rotational velocities (e.g. Ramírez-Agudelo et al. 2017; Sabín-Sanjulián et al. 2017) are intermediate between non-rotating and rapidly rotating models (40 per cent critical), and evidence points to a higher mass limit than 120 M$_\odot$ (Crowther et al. 2010; Brands et al. 2022).

We also make use of the latest CB19 grid of Charlot & Bruzual models (Bruzual & Charlot 2003; Plat et al. 2019), which employ non-rotating PARSEC stellar evolutionary tracks from Chen et al. (2015) calculated for a range of metallicities, synthetic hot luminous star templates from WM-Basic, TLUSTY (OB), and PoWR (WR) (Sánchez et al. 2022) with integrated populations drawn from either a Salpeter, Kroupa, or Chabrier IMF for stars up to $M_{\rm up}$ = 100, 300, or 600 M$_\odot$ (Sánchez et al. 2022).

Crucially, binary evolution is neglected in both Starburst99 and Charlot & Bruzual models, despite observational evidence indicating a high fraction of close binaries amongst massive stars at the LMC metallicity (Sana et al. 2013). Therefore, we also consider BPASS (v2.2.1; Eldridge et al. 2017; Stanway & Eldridge 2018) models incorporating binary evolution, a Kroupa IMF, and an upper mass limit of $M_{\rm up}$ = 100 or 300 M$_\odot$. Stellar atmosphere models incorporated into BPASS that are relevant for young populations are WM-Basic (O), PoWR (WR), and ATLAS (B).

The Hα equivalent width is a sensitive indicator of age for a young star burst. We measure W_λ (Hα) = 692 ± 24 Å. We initially focus on Z = 0.002 predictions from Starburst99 on the basis of the strong line calibrations, so adopt contemporary non-rotating models from Georgy et al. (2013). We obtain an age of 4.2 Myr, such that the Hα luminosity (Table 3) corresponds to a stellar mass of 5.5 × 10^4 M$_\odot$. Broadly similar results are obtained for historical Z = 0.008 models (Meynet et al. 1994) aside from a higher mass of 8.5 × 10^4 M$_\odot$. Comparable results are obtained from the Hβ equivalent width, W_λ (Hβ) = 97 ± 1Å. Revised ages accounting for underlying absorption in Hα − β are barely affected owing to the exceptionally strong Balmer emission.

[5] Z = 0.008 models appropriate for the LMC have only recently become available (Eggenberger et al. 2021)

Downloaded from https://academic.oup.com/mnras/article/527/3/9023/7455889 by guest on 16 February 2024

In reality the stellar population within NGC 2070 is not coeval – see (Schneider et al. 2018b, their fig. 4) and (Castro et al. 2021b, their fig. 10). In particular, the ages of OB stars within 1.2 arcmin of R136 (broadly comparable to MUSE pointing) span 1–7 Myr from comparison with evolutionary predictions for LMC metallicity OB stars (Brott et al. 2011), excluding the R136 star cluster whose age is ∼1.5 Myr (Crowther et al. 2016; Brands et al. 2022). Nevertheless, the median age of massive stars in NGC 2070 (3.6 Myr, Schneider et al. 2018b) is in good agreement with the age inferred from Hα using Z=0.002 or Z = 0.008 metallicity models.

3.3 WR properties

The spectral resolution of MUSE prevents the detection of photospheric absorption lines, but the high S/N does reveal broad WR bumps (Fig. 2). The blue bump is dominated by broad He II λ4686 (FWHM ∼ 25 Å, W_λ ∼ 6 Å), with no nebular component detected. Broad N III $\lambda\lambda$4634-41 is also observed, suggesting a dominant late WN population, while the yellow WR bump is dominated by C IV $\lambda\lambda$5801-12 (FWHM∼80 Å, W_λ ∼ 4 Å) from WC stars. The high S/N of our MUSE integrated data set unusually also permits broad He II 5411 emission to be detected. Optical emission line fluxes from individual stars are provided in table 2 of Castro et al. (2018).

Both classical WR stars and main sequence VMSs (WN5h and Of/WN) are major contributors to He II λ4686, with R136a contributing ∼20 per cent of the total, whereas the blend of N III $\lambda\lambda$4634–41 and C III $\lambda\lambda$4647–51 and C IV λ5801–20 are dominated by classical WR stars (primarily R140a). The presence of WR features in Starburst99, CB19, and BPASS synthetic spectroscopy provide independent age indicators (Schaerer & Vacca 1998). We require a non-standard extinction law in order to reconcile the UV and optical spectrophotometry of NGC 2070 with predictions. We adopt an LMC law with R_V = 4.5 (De Marchi & Panagia 2014; Maíz Apellániz et al. 2014; Brands et al. 2023) and obtain $E_{B\text{-}V}$ = 0.3 mag (A_V = 1.35 mag) for spectral energy distribution comparisons in the top panel of Fig. 7. Masses inferred from Starburst99, CB19, and BPASS stellar continua are 7.7×10^4 M$_\odot$, 6.5×10^4 M$_\odot$, and 11×10^4 M$_\odot$, respectively, in reasonable agreement with L(Hα) derived masses. The nebular continuum is not included in Fig. 7 since it has a negligible contribution to the far-UV and Paschen continua.

Z = 0.002 metallicity models predict extremely weak WR emission for all population synthesis models. Consequently, we adopt more realistic Z = 0.008 models for age determinations based on WR stars, although different models have different time resolutions (e.g. 1 Myr intervals for BPASS). The peak strength of optical WR bumps occurs at 4.2, 3, and 4 Myr for Starburst99, CP19, and BPASS models, respectively. Starburst99 models at solar metallicity (Z = 0.014; Ekström et al. 2012) allow comparisons between peak WR ages associated with non-rotating (4.5 ± 0.5 Myr) and rotating (5 ± 2 Myr) models.

We compare the Starburst99 synthetic spectrum associated with the 4.2 Myr age corresponding to the maximum WR population from the Meynet et al. (1994) evolutionary models in the central and bottom panels of Fig. 7, which coincide with the Hα-inferred age. Both WR bumps are predicted, albeit significantly weaker than observed for the He II λ4686 + N III $\lambda\lambda$4634-41 bump. It is clear that either the number of WR stars predicted from single star models at low metallicity or their line luminosities, or both, are underestimated (stronger emission is predicted for solar metallicity models). The synthetic spectrum also highlights strong photospheric absorption lines associated with Balmer lines.

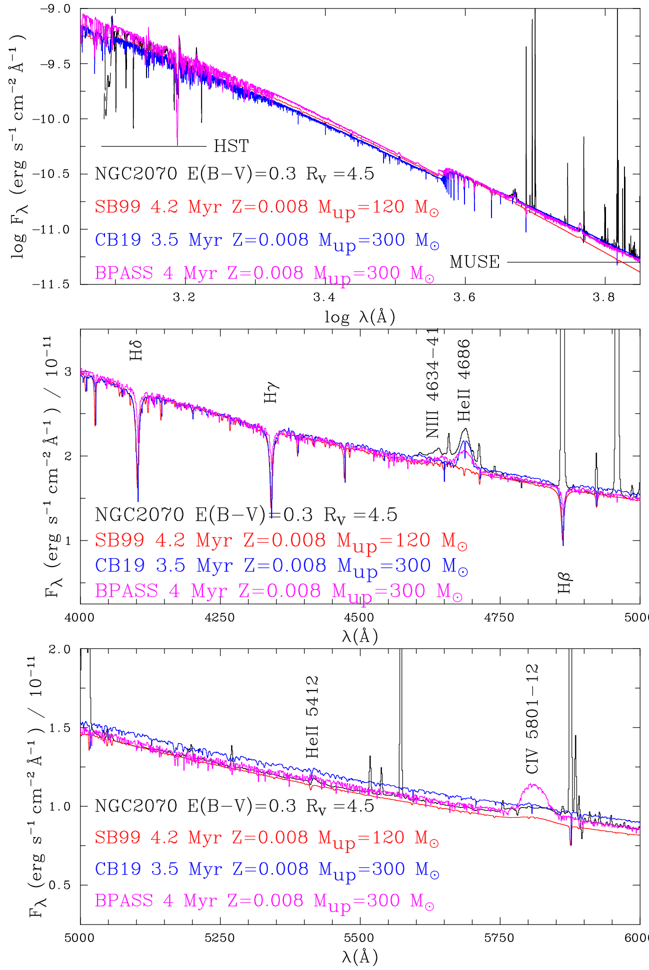

Figure 7. Top panel: Comparison between dereddened ($E_{B\text{-}V}$ = 0.3, R_V = 4.5) integrated UV and MUSE spectrum of the central region of NGC 2070 (black) and the predicted 4.2 Myr Starburst99 spectra (red) based on Z = 0.008 metallicity evolutionary models extending to M_{up} = 120 M$_\odot$ (Meynet et al. 1994), plus predicted 3.5 Myr CB19 spectra (blue) based on Z = 0.008 metallicity evolutionary predictions (Chen et al. 2015) extending to M_{up} = 300 M$_\odot$ and predicted 4 Myr BPASS spectra (pink) also based on Z = 0.008 predictions (Eldridge et al. 2017) for single stars extending to M_{up} = 300 M$_\odot$. Central panel: Zoom including blue WR bump (He II λ4686 and N III $\lambda\lambda$4634-41. A weak bump is predicted in the Starburst99 model, with improved agreement obtained from CB19 and BPASS models (similar WR emission is predicted for M_{up} = 100 M$_\odot$). Bottom panel: Zoom including yellow WR bump (C IV $\lambda\lambda$5801-12). The 4.2 Myr Starburst99 model is a good match to the yellow bump, whereas this feature is too weak in CB19 and too strong in BPASS. Weak stellar He II λ5412 is also observed in the MUSE data set. Emission lines not explicitly labelled are nebular (Hβ, [O III] λ4959, 5007, He I λ5876).

In contrast, the 3.5 Myr CB19 synthetic spectrum (blue) based on PARSEC evolutionary models at Z = 0.008 with M_{up} = 300 M$_\odot$ (Chen et al. 2015) provides a stronger He II λ4686 emission in the central panel of Fig. 7, albeit too weak and with negligible N III $\lambda\lambda$4634-41 and C IV $\lambda\lambda$5801-12 emission in lower panel. This age is close to the median 3.6 Myr age of massive stars in NGC 2070 according to Schneider et al. (2018b). Comparable WR emission is predicted at this age for CB19 models with M_{up} = 100 M$_\odot$, since VMSs have somewhat shorter lifetimes.

For the BPASS single star models with M_{up} = 300 M$_\odot$, WR emission is most prominent at 4 Myr, with comparable C IV $\lambda\lambda$5801-12

Downloaded from https://academic.oup.com/mnras/article/527/3/9023/7455889 by guest on 16 February 2024

emission predicted (too strong), and a higher He II λ4686 equivalent width, albeit comparable to predictions from CB19 models (central and bottom panels of Fig. 7). The Hα luminosity at this age for the $M_{\rm up} = 300 M_\odot$ model corresponds to a stellar mass of ∼6 × 10^4 $M_\odot$.

Alternatively, it is possible to empirically estimate WR populations if line luminosity calibrations are available (Schaerer & Vacca 1998). Assuming the blue bump is dominated by WN stars, one obtains a population of ∼20 WN6–8 stars (or 12 WN5–7h stars) based on the latest WR line luminosities at the LMC metallicity from Crowther et al. (2023). The yellow bump is dominated by WC stars, from which a population of 4 WC4–5 stars is obtained. In reality, WC stars also contribute 15 per cent to the blue bump via C III λ4650 and He II λ4686. Consequently the inferred number of WN stars is reduced to 17 WN6–8 stars (or 10 WN5–7h stars). These calibrations are within a factor of two of the known population (11 WN stars, 2 WC4 including individual components of multiple WR systems R140a and Mk 34).

4 ANALYSIS OF INTEGRATED FAR-UV SPECTROSCOPY

In common with previous studies of young extragalactic stellar populations in the UV, we again utilize predictions of the emergent far-UV spectrum from the population synthesis tool Starburst99 (version 7.0.1; Leitherer et al. 1999, 2014), Charlot & Bruzual (CB19, Bruzual & Charlot 2003; Plat et al. 2019), and BPASS (v2.2.1, Eldridge et al. 2017; Stanway & Eldridge 2018) once our empirical data set has been dereddened according to an LMC extinction law with $R_V = 4.5$ and $E_{B-V} = 0.3$ mag, as for the optical comparison. The λ1500 luminosity of the NGC 2070 empirical data set corresponds to $\log L_{\rm FUV} = 38.04$ erg s^{-1}.

Strong interstellar Lyα absorption impacts the observed N V λλ1238-42 profile (e.g. Wofford et al. 2023, their fig. 3). We have estimated $\log N$(H I) cm^{-2} = 21.75 ± 0.05 from Lyα fits to COS/G130M and STIS/E140M observations of individual stars within the MUSE field of view (Table C1). However, application to theoretical predictions leads to a suppressed continuum extending to ∼1300 Å, contrary to observations. This is because LMC templates, which dominate the cumulative far-UV spectrum, span a broad range of N(H I) column densities (Welty, Xue & Wong 2012). Consequently, no corrections to Lyα have been applied, of relevance to detailed comparisons between observed and predicted N V λλ1238-42 profiles.

Once again, although the optical strong line calibrations favour an unphysical SMC-like metallicity, we discuss both Z = 0.002 and Z = 0.008 metallicity predictions in the far-UV in order to test predictions. We limit our discussion to single bursts, although in reality NGC 2070 and other far-UV observations involve a mixed population. Dual or multiple age populations are occasionally implemented for spectral fitting (e.g. Chisholm et al. 2019; Sirressi et al. 2022), but NGC 2070 comprises a star cluster embedded within an extended (spatially and temporally) star-forming region.

4.1 Starburst99

The primary age indicators in the far-UV are N V λλ1238–42, Si IV λλ1393–1402, and C IV λλ1548–51 for metal-poor populations with Starburst99 since empirical LMC/SMC stellar libraries cutoff at λ1600, preventing spectral comparisons for He II λ1640, although predicted equivalent widths of several WR lines are available, including He II λ1640. The maximum He II λ1640 emission occurs at an age of 3.2 Myr for the Z = 0.002 (Georgy et al. 2013) Starburst99 model. Fig. 8 provides a comparison between this model and dereddened NGC 2070 spectrum, revealing a good match to N V λλ1238–42, a weak P Cygni C IV λλ1548–51 profile, and a somewhat too weak Si IV λλ1393–1402 wind signature. He II λ1640 represents a major discrepancy, since the predicted emission of W_λ = 0.01 Å, is negligible with respect to the observed strength (W_λ = 4.7 ± 0.2 Å).

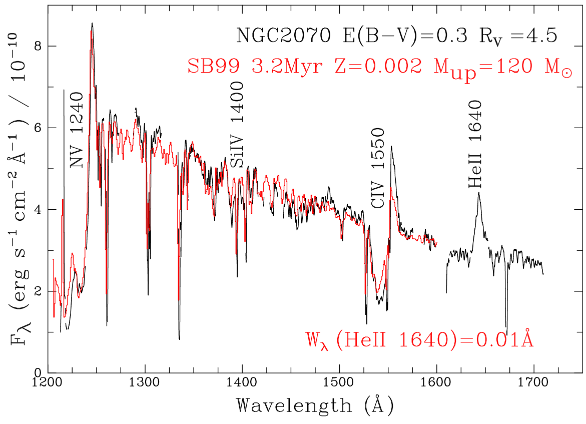

Figure 8. Comparison between dereddened (E_{B-V} = 0.3, R_V = 4.5) cumulative far-UV spectrum of the central region of NGC 2070 (black) and the predicted Starburst99 spectrum based on Z = 0.002 evolutionary models (Georgy et al. 2013) with LMC/SMC UV templates at 3.2 Myr (red). Far-UV luminosities for this age correspond to stellar masses of 5 × 10^4 $M_\odot$. The cutoff at λ1600 is due to the use of empirical templates (predicted He II λ1640 emission equivalent width is indicated).

In view of the overall poor match to observations at Z = 0.002, in Fig. 9, we compare the dereddened NGC 2070 spectrum to predictions for non-rotating Z = 0.008 metallicity models (Meynet et al. 1994) plus LMC/SMC empirical templates at 3 Myr (start of WR emission) and 4.2 Myr (peak WR emission). At 3 Myr, results are broadly similar to the Z = 0.002 case, whereas at 4.2 Myr (Hα-inferred age from Section 3.2), the P Cygni Si IV λλ1393–1402 is well reproduced owing to OB supergiants being present in sizeable numbers, but the strength of both the N V λλ1238–42 and C IV λλ1548–51 P Cygni profiles are underpredicted. The He II λ1640 emission strength remains underestimated, albeit with an improved predicted equivalent width of 1.5 Å.

Overall, metal-poor Starburst99 models fare rather poorly in quantitatively reproducing the empirical data set. The origin of this disagreement has multiple causes:

(i) The central region of NGC 2070 is not a coeval burst, since it hosts a young, potentially coeval, star cluster R136 contributing 1/3 of the far-UV continuum (Fig. 5) with the remainder spanning ages of 1–7 Myr (Schneider et al. 2018b). Improved agreement could be obtained by adopting dual age populations representing the cluster and extended star-forming region.

(ii) NGC 2070 is host to a number of VMS, within R136 and beyond, which possess very strong winds owing to their proximity to the Eddington limit (Bestenlehner 2020; Brands et al. 2022). These stars produce strong He II λ1640 emission while on the main sequence (Crowther et al. 2016). In addition, we have shown that VMS contribute 18 per cent of the far-UV continuum of NGC 2070, such that models with upper mass cutoffs at ∼100 $M_\odot$ will underestimate the far-UV continuum. In order to reproduce He II λ1640 in very young populations, one needs to extend the IMF in population

Downloaded from https://academic.oup.com/mnras/article/527/3/9023/7455889 by guest on 16 February 2024

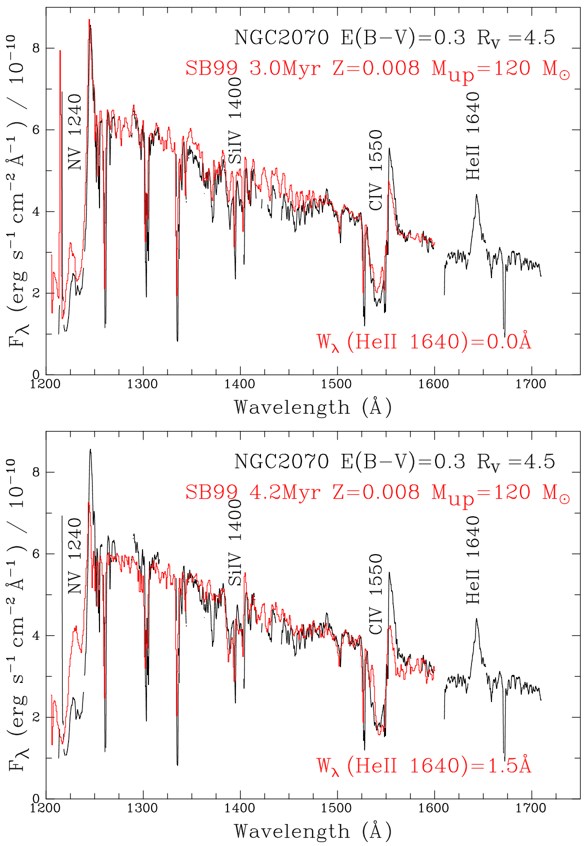

Figure 9. Comparison between dereddened ($E_{\rm B\text{-}V}$ = 0.3, $R_{\rm V}$ = 4.5) cumulative far-UV spectrum of the central region of NGC 2070 (black) and the predicted Starburst99 spectrum (red) based on Z = 0.008 metallicity evolutionary models (Meynet et al. 1994) at 3.0 Myr (upper panel) and 4.2 Myr (lower panel) with LMC/SMC UV templates. Far-UV luminosities for this range of ages correspond to stellar masses of 5.5–8.5 × 10^4 M$_\odot$. The cutoff at λ1600 is due to the use of empirical templates (predicted He II λ1640 emission equivalent width is indicated).

synthesis calculations to higher masses and incorporate revised mass-loss prescriptions (Wofford et al. 2023).

(iii) The empirical UV template spectra at low metallicity in Starburst99 are a mix of SMC and LMC stars, since these were incorporated at a time prior to the availability of large numbers of high-quality far-UV templates (Roman-Duval et al. 2020). OB stars in the SMC possess significantly weaker winds than LMC counterparts (Prinja & Crowther 1998; Mokiem et al. 2007), so the use of SMC templates will yield weaker P Cygni profiles than observations at LMC composition. Alternatively, theoretical spectra could lead to improved agreement (e.g. Leitherer et al. 2010), especially at low metallicities where empirical templates are scarce or unavailable.

(iv) It is well known that evolutionary models for single stars struggle to reproduce observed WR populations (Hamann et al. 2019). In reality, binary channels (including mergers) will increase the production of WR and lower mass He stars, which will enhance the strength of He II λ1640 from all WR subtypes, as well as other far-UV P Cygni profiles (N V λλ1238–42 from WN stars, C IV λλ1548–51 from WC stars).

Previous analyses of extragalactic star clusters (e.g. Smith et al. 2016; Sirressi et al. 2022) or entire galaxies (e.g. James et al. 2014; Chisholm et al. 2019) are often more successful at reproducing far-

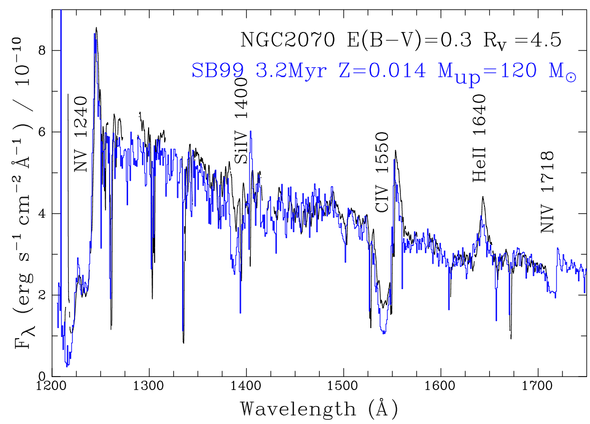

Figure 10. Comparison between dereddened ($E_{\rm B\text{-}V}$ = 0.3, $R_{\rm V}$ = 4.5) cumulative far-UV spectrum of the central region of NGC 2070 (black) and the predicted Starburst99 spectrum based on contemporary, non-rotating Z = 0.014 evolutionary models (Ekström et al. 2012) plus empirical Milky Way UV templates at 3.2 Myr (blue). The Far-UV luminosity of this model corresponds to a stellar masses of 6 × 10^4 M$_\odot$.

UV observations than we have achieved for NGC 2070, albeit not universally so (Sidoli, Smith & Crowther 2006; Wofford et al. 2014; Leitherer et al. 2018). In part, this is achieved since the metallicity is varied, with high metallicities preferred in cases of strong stellar wind signatures, irrespective of nebular results for the regions in question.

To illustrate the role played by metallicity, we compare the dereddened UV spectrum of NGC 2070 with prediction of a 3.2 Myr model at Z = 0.014 (Ekström et al. 2012) plus *Milky Way* UV templates in Fig. 10. In contrast to Fig. 9, N V λλ1238–42, C IV λλ1548–51, and He II λ1640 are now reasonably well predicted, with Si IV λλ1393–1402 a little too strong and the far-UV iron forest also over predicted. N IV λ1718 is also prominent (recall Fig. 6), in contrast to metal-poor predictions. Nevertheless, the overall match is satisfactory for an age close to the median of OB stars in NGC 2070 (Schneider et al. 2018b), albeit reliant on unphysical evolutionary models and templates.

4.2 Charlot and Bruzual

The extension of Charlot & Bruzual 2019 models to IMFs with high upper mass limits at a wide range of metallicities permits some deficiencies of current Starburst99 models to be addressed. As demonstrated by Wofford et al. (2023), the difference in predicted He II λ1640 emission at ages of 1–3 Myr between $M_{\rm up}$ = 100 and 300 M$_\odot$ at LMC metallicity (Z = 0.008) is striking (their fig 4). This arises from the inclusion of mass-loss prescriptions for VMSs (Vink et al. 2011). We compare far-UV CB19 (Z = 0.002, Kroupa IMF) predictions for $M_{\rm up}$ = 100 and 300 M$_\odot$ at 1.0 and 2.5 Myr with NGC 2070 observations in Fig. 11. These ages correspond to the maximum He II λ1640 emission due to VMSs (1 Myr) and classical WR stars (2.5 Myr) for $M_{\rm up}$ = 300 M$_\odot$. At 1 Myr, the high upper mass limit prediction provides a closer agreement with observations, albeit with O V λ1371 too strong, He II λ1640 too weak and C IV λλ1548–51 extremely weak. At 2.5 Myr, all wind features are far too weak, with the exception of He II λ1640 for the $M_{\rm up}$ = 300 M$_\odot$ case which has a satisfactory emission equivalent width, albeit far broader than observed.

Consequently, we also consider Z = 0.008 predictions from CB19 with $M_{\rm up}$ = 100 and 300 M$_\odot$. Fig. 12 compares predictions at 2.2,

Downloaded from https://academic.oup.com/mnras/article/527/3/9023/7455889 by guest on 16 February 2024

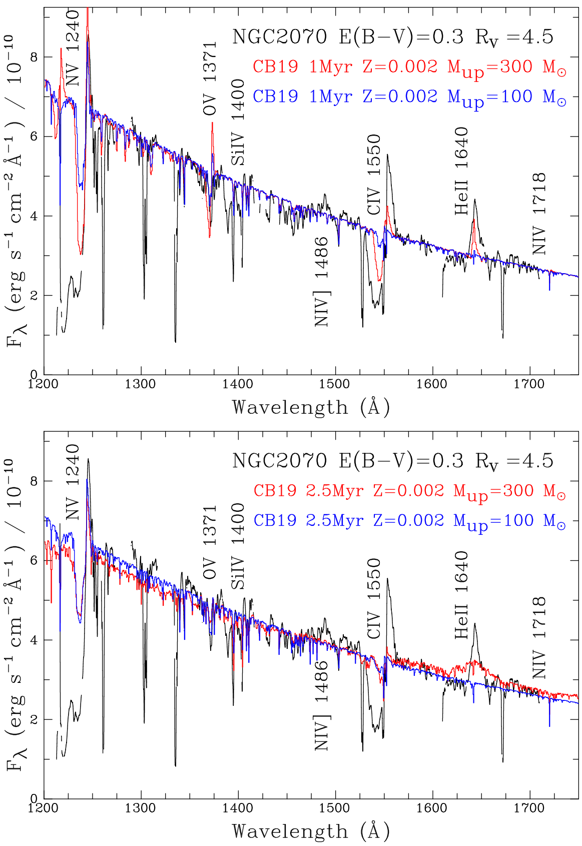

Figure 11. Comparison between dereddened ($E_{\rm B\text{-}V}$ = 0.3, R_V = 4.5) cumulative far-UV spectrum of the central region of NGC 2070 (black) and the predicted CB19 spectrum based on Z = 0.002 evolutionary models (Chen et al. 2015) with $M_{\rm up}$ = 300 $M_\odot$ (red) or 100 $M_\odot$ (blue) at 1.0 Myr (top panel) and 2.5 Myr (lower panel). Far-UV luminosities for this range of ages correspond to stellar masses of 5–8 × 10^4 $M_\odot$ for the $M_{\rm up}$ = 300 $M_\odot$ models.

3.0, and 3.8 Myr with observations, which span the range of ages at which prominent He II λ1640 emission is predicted. At all ages the $M_{\rm up}$ = 300 $M_\odot$ model provides a better match to observations. Wofford et al. (2023, their fig. 4) highlight the sharp peak in He II λ1640 at 2.2 Myr once VMSs enter the late WN phase (see also Smith et al. 2023). Consequently, the predicted He II λ1640 is in good agreement with observations at this precise age, as is C IV λ1550, albeit with O V λ1371 overpredicted, and Si IV λλ1393–1402 underpredicted. N IV] λ1486 is observed in NGC 2070, though is overpredicted in models at this age that extend to $M_{\rm up}$ = 300 $M_\odot$.

Turning to later ages, O V λ1371 has faded in strength after 3 Myr, with Si IV λλ1393–1402 now well reproduced, with He II λ1640 emission a little too weak, with C IV λλ1548–51 also too weak, alongside Si IV λ1640. C IV λλ1548–51 continues to weaken at later ages (3.8 Myr) with He II λ1640 from classical WR stars now well reproduced and Si IV λλ1393–1402 still matched. Overall, use of CB19 models at Z = 0.008 favour an age of 2.2 Myr for NGC 2070 plus a high upper mass limit, in spite of the poor match to O V λ1371 and very weak N IV λ1718 (in contrast to *IUE* observations in Fig. 6).

4.3 BPASS

Finally, we consider BPASS (v.2.2.1; Eldridge et al. 2017; Stanway & Eldridge 2018) models for single or binary populations at Z = 0.002 and Z = 0.008, with a Kroupa IMF and $M_{\rm up}$ = 300 $M_\odot$. The maximum

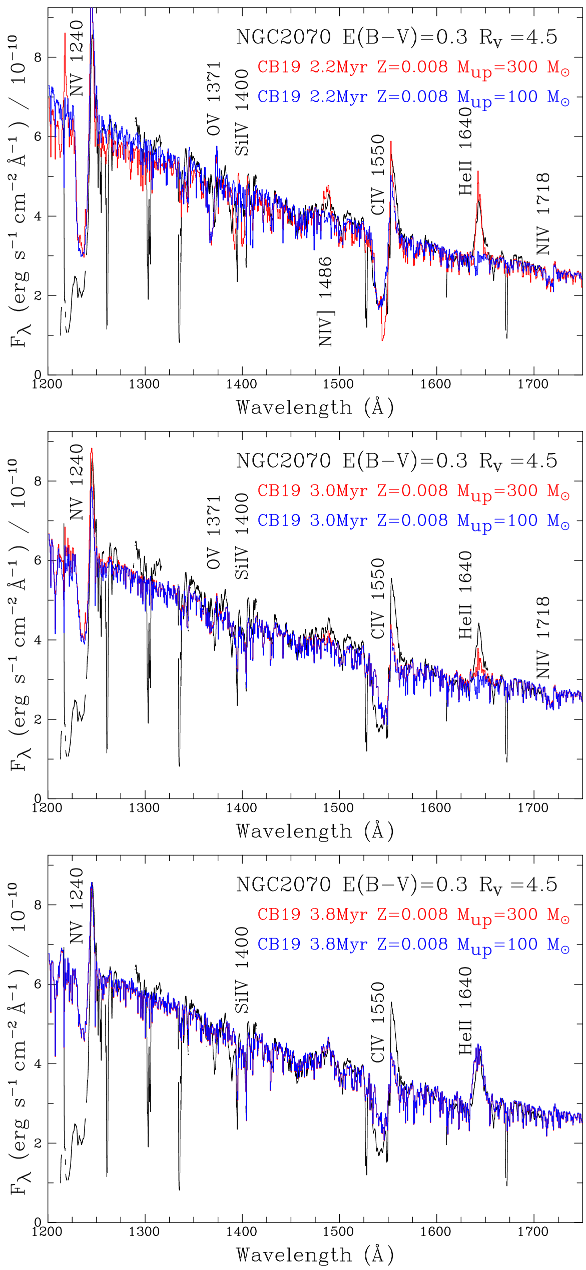

Figure 12. Comparison between dereddened ($E_{\rm B\text{-}V}$ = 0.3, R_V = 4.5) cumulative far-UV spectrum of the central region of NGC 2070 (black) and the predicted CB19 spectrum based on Z = 0.008 evolutionary models (Chen et al. 2015) with $M_{\rm up}$ = 300 $M_\odot$ (red) or 100 $M_\odot$ (blue) at 2.2 Myr (top panel), 3.0 Myr (central panel), and 3.8 Myr (lower panel). Far-UV luminosities for this range of ages correspond to stellar masses of 4–9 × 10^4 $M_\odot$ for the $M_{\rm up}$ = 300 $M_\odot$ models.

He II λ1640 emission at Z = 0.002 is predicted at an age of 4 Myr (single or binary case), as shown in Fig. 13. At this metallicity, all wind lines are predicted to be too weak, albeit with He II λ1640 only a factor of two weaker than observed, since several H-rich WN stars are predicted for cluster mass of 9 × 10^4 $M_\odot$ which reproduces the far-UV luminosity of NGC 2070. At Z = 0.008, predictions are improved, as shown in Fig. 14 for ages of 2 Myr (upper panel) and 4 Myr (lower panel). For the 2 Myr case, C IV λλ1548–51, N V λλ1238–42, and Si IV λλ1393–1402 are reasonably well reproduced, although He II λ1640 emission is only weakly present despite the

Downloaded from https://academic.oup.com/mnras/article/527/3/9023/7455889 by guest on 16 February 2024

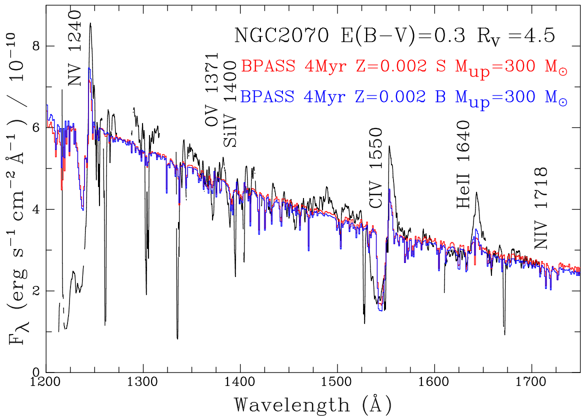

Figure 13. Comparison between dereddened ($E_{\rm B\text{-}V}$ = 0.3, $R_{\rm V}$ = 4.5) cumulative far-UV spectrum of the central region of NGC 2070 (black) and the predicted BPASS spectrum based on Z = 0.002 metallicity evolutionary models (v.2.2.1, Eldridge et al. 2017) at 4 Myr for single stars (red) and binaries (blue). Far-UV luminosities correspond to stellar masses of 9 × 10^4 M$_\odot$ for the binary models.

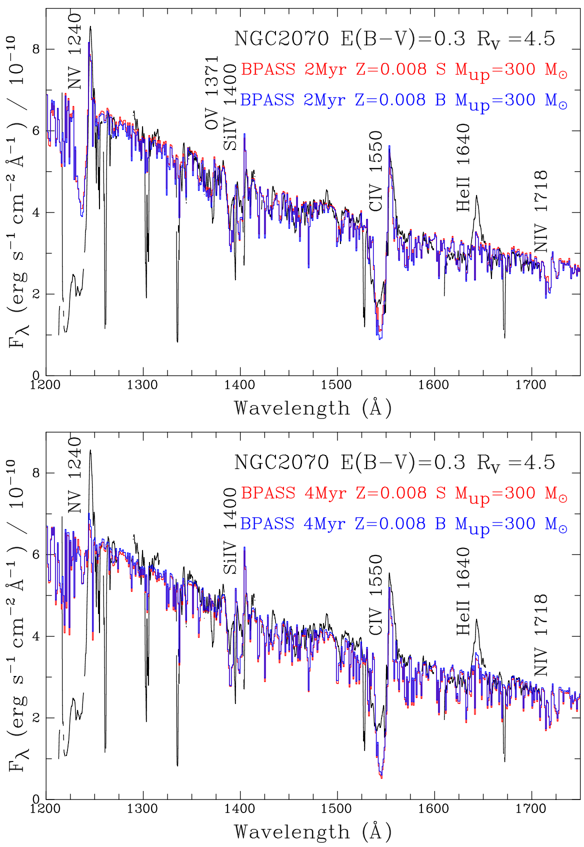

Figure 14. Comparison between dereddened ($E_{\rm B\text{-}V}$ = 0.3, $R_{\rm V}$ = 4.5) cumulative far-UV spectrum of the central region of NGC 2070 (black) and the predicted BPASS spectrum based on Z = 0.008 metallicity evolutionary models (v.2.2.1, Eldridge et al. 2017) at 2 Myr (upper panel) and 4 Myr (lower panel) for single stars (red) and binaries (blue). Far-UV luminosities for this range of ages correspond to stellar masses of 5–9 × 10^4 M$_\odot$ for the binary models.

Table 4. Summary of results for individual versus integrated treatment of NGC 2070 in UV and visual, with integrated results obtained from Starburst99 (SB99) using Z = 0.008 evolutionary models (Meynet et al. 1994) and $M_{\rm up}$ = 120 $M_\odot$, Charlot & Bruzual (CB19) using Z = 0.008 evolutionary models (Chen et al. 2015) and $M_{\rm up}$ = 100 or 300 M$_\odot$ or BPASS Z = 0.008 single and binary models (v.2.2.1, Eldridge et al. 2017; Stanway & Eldridge 2018). LMC WR template luminosities are from Crowther, Rate & Bestenlehner (2023) while N2 and O3N2 strong line calibrations are from Curti et al. (2017).

Property	Individual	Ref	Integrated	This study
			Visual (MUSE)	
Age (Myr)	1–7, 1–2.5†	a,b	4.2, 3.0, 4	SB99, CB19, BPASS
Mass (10^5M$_\odot$)	0.5–1.0	c,d	0.85, 0.6, 1.1	SB99, CB19, BPASS
$M_{\rm up}$(M$_\odot$)	∼270	b	100–300	CB19
N(WN)	11	e	10–17	WR templates
N(WC4)	2	e	4	WR templates
log (O/H) + 12	8.26–8.5	f,g	7.9–8.1	N2, O3N2 diagnostics
			Far-UV (HST)	
Age (Myr)	1.5†	h	4.2, 2.2, 2	SB99, CB19, BPASS
Mass (10^5M$_\odot$)	···	···	0.85, 0.4, 0.5	SB99, CB19, BPASS
$M_{\rm up}$(M$_\odot$)	∼250	h	300	CB19
Z	···	···	0.014	SB99‡

a: Schneider et al. (2018b); b: Brands et al. (2022); c: Hunter et al. (1995); d: Andersen et al. (2009); e: Doran et al. (2013); f: Vermeij & van der Hulst (2002); g: Peimbert (2003); h: Crowther et al. (2016)

‡ Z = 0.014 models (Ekström et al. 2012) and Milky Way templates † R136 cluster

inclusion of VMSs, and N IV λ1718 is very weak (in contrast with *IUE* observations in Fig. 6).

Binary models predict ∼6 VMSs at 2 Myr for a stellar mass of 5 × 10^4 M$_\odot$ that reproduces the far-UV luminosity of NGC 2070, categorized as a mix of O, Of and H-rich WN-types. In contrast with CB19 models, BPASS mass-loss prescriptions fail to account for the proximity of VMSs to the Eddington limit (Bestenlehner 2020; Brands et al. 2023). Predictions from single models are very similar to those from binary stars at such ages. At 4 Myr, preferred from predicted optical WR bumps, N V λλ1238–42 is now too weak, Si IV λλ1393–1402 is too strong, with He II λ1640 again too weak despite arising from classical WR stars. A stellar mass of 9 × 10^4 M$_\odot$ is required for the binary models to reproduce the far-UV luminosity of NGC 2070 at 4 Myr, with ∼10 classical WR stars predicted (mix of WN and WC). Overall, the 2 Myr BPASS models (single or binary) provide the closest match to UV observations, aside from the weakness of He II λ1640.

5 DISCUSSION AND CONCLUSIONS

We present the integrated VLT/MUSE spectrum of the central 2 × 2 arcmin^2 (30 × 30 pc^2) region of NGC 2070, the dominant giant H II region of the Tarantula (30 Doradus) region in the LMC and construct an empirical far-UV spectrum of this region by combining observations of individual stars with templates from the ULLYSES survey (Roman-Duval et al. 2020). This region is unique in the sense that we are able to compare results from an individual treatment of stars with an integrated approach, plus both classical Wolf-Rayet stars and VMS have been identified within this region. A summary of UV and optical results is presented in Table 4.

Martins et al. (2023) consider UV and optical spectroscopic indicators of WR and VMSs in nearby star-forming regions, favouring optical diagnostics to identify the latter. Neither the far-UV (HST) nor optical (MUSE) spectroscopy of NGC 2070 permit unique diagnostics of VMS since both populations have similar He II λ1640 morphologies (Fig. 4) and metal lines in the vicinity of He II λ4686 are dominated by classical WR stars (Fig. 2). Consequently, despite NGC 2070 having the richest VMS population in the Local Group, their presence is masked by its mixed age population, which includes

Downloaded from https://academic.oup.com/mnras/article/527/3/9023/7455889 by guest on 16 February 2024

classical WR stars. Nevertheless, unambigious diagnostics of very young populations (required for VMS) exist in the optical (Martins et al. 2023) and far-UV (Crowther et al. 2016), the latter involving the presence of P Cygni O V λ1371 and He II λ1640 emission with Si IV λλ1393-1402 absent.

If we were reliant solely on integrated visual spectroscopy of NGC 2070, we would substantially underestimate its metallicity from strong line diagnostics (Marino et al. 2013; Curti et al. 2017) but obtain an age of the stellar population (∼4 Myr from Starburst99 and BPASS, 3.5 Myr from CB19) in close agreement with the median age of massive stars within the region. The Starburst99 inferred mass is broadly consistent with that of the star cluster R136 (Hunter et al. 1995; Andersen et al. 2009) that likely dominates the stellar mass of the region. The strength of WR bumps from historical LMC metallicity models (Meynet et al. 1994) implemented in Starburst99 are underestimated, although results from contemporary LMC models (Chen et al. 2015) plus a high $M_{\rm up}$ = 300 $M_{\odot}$ in CB19 and BPASS models are improved for He II λ4686 and C IV λλ5801-12. The number of WR stars estimated from line luminosities of blue and yellow WR bumps is in good agreement with latest empirical calibrations for LMC metallicity (Crowther et al. 2023).

Starburst99 predictions from Z = 0.008 metallicity evolutionary models (Meynet et al. 1994) plus Magellanic Cloud empirical UV templates are incapable of reproducing the primary wind features in the integrated far-UV spectrum of NGC 2070 at a single age. For example, the maximum predicted emission W_{λ}(He II λ1640) = 1.5 Å, a factor of three lower than observed (4.7 ± 0.2 Å). Starburst99 models using contemporary solar metallicity models (Ekström et al. 2012) and Milky Way templates at 3.2 Myr provide a better match despite an unphysical metallicity. Various reasons for these deficiencies are set out in Section 4, including the mixed age of massive stars contributing to the integrated light (only 1/5 arises from the R136 cluster), plus the lack of high-quality empirical templates (e.g. ULLYSES, Roman-Duval et al. 2020), neglect of VMSs and the lack of binary evolutionary models.

CB19 models accounting for Z = 0.008 evolutionary models (Chen et al. 2015) and synthetic spectra are more successful at reproducing He II λ1640 emission at 2.2 Myr since they extend to higher initial masses $M_{\rm up}$ = 300 $M_{\odot}$) and fold in contemporary mass-loss prescriptions for VMSs, although no single age provides a satisfactory solution for all UV diagnostics. BPASS (Eldridge et al. 2017) models incorporate binary evolution but do not currently incorporate enhanced mass-loss for VMSs resulting from their proximity to the Eddington limit. Consequently, BPASS models are unable to reproduce strong He II λ1640 in metal-poor models even with $M_{\rm up}$ = 300 $M_{\odot}$).

Fixing Z = 0.008 and combining UV and optical spectroscopic diagnostics, Starburst99 models at ∼4.2 Myr are capable of reproducing some optical (Hα, C IV λλ5801-12) and UV (Si IV λλ1393-1402) features of NGC 2070, although He II λ1640, λ4686 and C IV λλ1548–51 are too weak. CB19 models at 3.8 Myr provide a better match to He II λ1640 and λ4686, although C IV λλ1548–51 and λλ5801-12 are too weak, while BPASS models at 4 Myr underpredict He II λ1640, λ4686, overpredicts C IV λλ58012-12, with Si IV λλ1393-1402 and C IV λλ1548-51 broadly satisfactory. In view of our results, caution should be given to specific ages and metallicities of young, unresolved stellar populations (see Martins & Palacios 2022; Wofford et al. 2023). Should observed regions include multiple star clusters or clusters embedded within extended star-forming regions, it would be more realistic to incorporate either a dual or multiple populations (e.g. Chisholm et al. 2019; Sirressi et al. 2022), although the extended population of NGC 2070 is far from coeval (Schneider et al. 2018b).

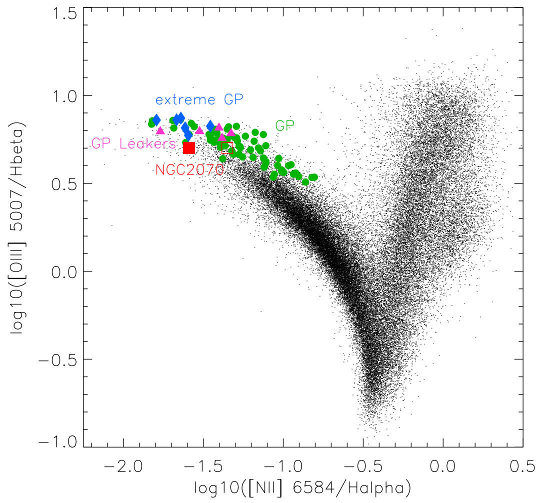

Figure 15. BPT diagram (Baldwin, Phillips & Terlevich 1981) illustrating the similarity in integrated strengths between NGC 2070/Tarantula (filled/open red square), Green Pea (green circles), extreme Green Pea (blue diamonds), and Lyman-continuum emitting Green Pea (pink triangles) galaxies, together with plus SDSS star-forming galaxies (black dots, Abazajian et al. 2009), adapted from Micheva et al. (2017, their fig. 2) and Crowther et al. (2017).

Although NGC 2070 is located in the LMC, our nearest extragalactic star-forming galaxy, if one compares its nebular properties in the BPT diagram (Baldwin, Phillips & Terlevich 1981), it is located close to extreme Green Pea galaxies (Cardamone et al. 2009) as shown in Fig. 15. Green Pea galaxies have received considerable interest since a subset have been established as Lyman continuum leakers (Izotov et al. 2016). Hα observations of NGC 2070 (Fig. 1) suggests a significant fraction of ionizing photons escape the region. By way of example, BPASS models at 4 Myr favour a stellar mass of 8.5–11 × 10^4 $M_{\odot}$ from FUV-optical continua, but only 6 × 10^4 $M_{\odot}$ from its Hα luminosity, favouring a sizeable escape fraction of ionizing photons (see also Doran et al. 2013).

The relatively high star-formation rate of NGC 2070 for its size is also more comparable to the properties of star-forming knots at high redshift with respect to local star-forming galaxies (Kennicutt R. C. et al. 2003), as shown in Fig. 16. Specifically, NGC 2070 properties are close to clumps in the lensed galaxy SDSS J1110 + 6459 at z ∼2.5 (Johnson et al. 2017). Star-forming knots in the lensed Sunburst arc have a similar size to NGC 2070 but are significantly more intensive (Rivera-Thorsen et al. 2017, 2019; Vanzella et al. 2022).

As we have shown, the ULLYSES survey (Roman-Duval et al. 2020) provides high-quality far-UV empirical templates for OB stars at half-solar metallicity, which serve as alternatives to widely used theoretical models (Leitherer et al. 2010) in population synthesis tools. High-quality optical VLT/Shooter spectroscopy of ULLYSES targets has also been acquired (XshootU, Vink et al. 2023), which complement the present MUSE observations since templates achieve higher spectral resolution, extend to the violet, and complement existing optical spectroscopic libraries of massive stars (e.g. Verro et al. 2022).

Indeed, ULLYSES/XshootU spectroscopy have been secured for a large number of OB stars in the SMC. Ideally, we would wish to extend this study to the 1/5 solar metallicity of the SMC. The richest young star formation region in the SMC is NGC 346 (Massey,

Downloaded from https://academic.oup.com/mnras/article/527/3/9023/7455889 by guest on 16 February 2024

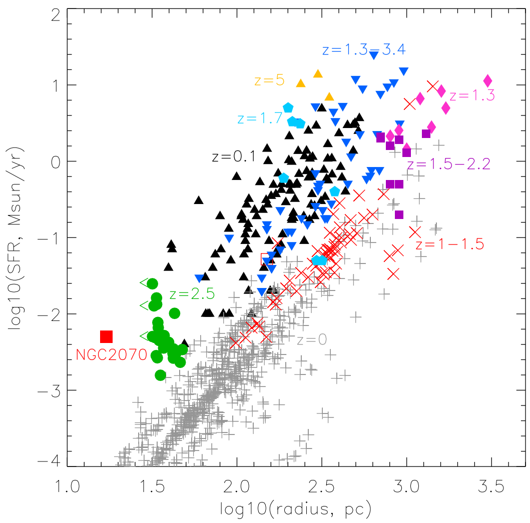

Figure 16. Comparison between the integrated star-formation rate of NGC 2070/Tarantula (filled/open red square) and star-forming knots from local star-forming galaxies ($z = 0$, grey Kennicutt et al. 2003) to those at a range of redshifts ($z = 0.1$–5), adapted from Johnson et al. (2017, their fig. 2) and Crowther et al. (2017).

Parker & Garmany 1989). STIS/G140L spectroscopy has recently been obtained for the O stars within the central region of this giant H II region (Rickard et al. 2022), whose central 1 × 1 arcmin^2 (20 × 20 pc^2) has been observed with VLT/MUSE. Unfortunately, NGC 346 lacks a massive young star cluster at its heart such that any analysis would need to reflect stochasticity in both its star formation history and IMF (e.g. da Silva, Fumagalli & Krumholz 2014; Krumholz et al. 2015; Orozco-Duarte et al. 2022).

Nevertheless, there are other large star-forming complexes in the Magellanic Clouds (Evans et al. 2006), for which quantitative UV-optical analysis could be undertaken based on ULLYSES templates plus integral field observations from the upcoming SDSS-V Local Volume Mapper (LVM, Kollmeier et al. 2017).

ACKNOWLEDGEMENTS

This study has been made possible courtesy of: (i) Science Verification MUSE observations of NGC 2070 (proposal led by Jorge Melnick and Chris Evans); (ii) the Director's Discretionary ULLYSES survey, which was implemented by a Space Telescope Science Institute (STScI) team led by Julia Roman-Duval, having been recommended by the Hubble UV Legacy Science Definition Working Group chaired by Sally Oey, convened in 2018 by the then STScI Director Ken Sembach. Thanks to Linda Smith for providing useful comments on a draft version of the manuscript, and the referee for feedback which helped to improve the clarity of the paper.

Based on observations made with ESO telescopes at the Paranal observatory under programme ID 60.A-9351(A) and observations obtained with the NASA/ESA Hubble Space Telescope, retrieved from the Mikulski Archive for Space Telescopes (MAST) at the STScI. STScI is operated by the Association of Universities for Research in Astronomy, Inc. under NASA contract NAS 5-26555. PAC is supported by the Science and Technology Facilities Council research grant ST/V000853/1 (PI. V. Dhillon). NC gratefully acknowledges funding from the Deutsche Forschungsgemeinschaft (DFG) CA 255/1-1.

This research has made use of the SIMBAD database, operated at CDS, Strasbourg, France. Starlink software is currently supported by the East Asian Observatory. IRAF was distributed by the National Optical Astronomy Observatory, which was managed by the Association of Universities for Research in Astronomy (AURA) under a cooperative agreement with the National Science Foundation. For the purpose of open access, the author has applied a Creative Commons Attribution (CC BY) license to any Author Accepted Manuscript version arising.

DATA AVAILABILITY

The integrated MUSE and far-UV spectroscopy of NGC 2070 are available in ascii format (wavelength in Å, flux in erg s^{-1} cm^{-2} Å^{-1}) at 10.5281/zenodo.10204404.

REFERENCES

Abazajian K. N. et al., 2009, ApJS, 182, 543
Andersen M., Zinnecker H., Moneti A., McCaughrean M. J., Brandl B., Brandner W., Meylan G., Hunter D., 2009, ApJ, 707, 1347
Bacon R. et al., 2010, in McLean I. S., Ramsay S. K., Takami H., eds, Society of Photo-Optical Instrumentation Engineers (SPIE) Conference Series Vol. 7735, Ground-based and Airborne Instrumentation for Astronomy III. p. 773508, preprint (arXiv:2211.16795)
Baldwin J. A., Phillips M. M., Terlevich R., 1981, PASP, 93, 5
Bartzakos P., Moffat A. F. J., Niemela V. S., 2001, MNRAS, 324, 18
Berg D. A. et al., 2022, ApJS, 261, 31
Bestenlehner J. M., 2020, MNRAS, 493, 3938
Bestenlehner J. M. et al., 2014, A&A, 570, A38
Bestenlehner J. M. et al., 2020, MNRAS, 499, 1918
Bestenlehner J. M., Crowther P. A., Broos P. S., Pollock A. M. T., Townsley L. K., 2022, MNRAS, 510, 6133
Bosch G., Terlevich R., Melnick J., Selman F., 1999, A&AS, 137, 21
Brands S. A. et al., 2022, A&A, 663, A36
Brands S. A., de Koter A., Bestenlehner J. M., Crowther P. A., Kaper L., Caballero-Nieves S. M., Gräfener G., 2023, A&A, 673, A132
Brott I. et al., 2011, A&A, 530, A115
Bruzual G., Charlot S., 2003, MNRAS, 344, 1000
Cardamone C. et al., 2009, MNRAS, 399, 1191
Carnall A. C. et al., 2023, MNRAS, 518, L45
Castro N., Crowther P. A., Evans C. J., Mackey J., Castro-Rodriguez N., Vink J. S., Melnick J., Selman F., 2018, A&A, 614, A147
Castro N. et al., 2021a, The Messenger, 182, 50
Castro N. et al., 2021b, A&A, 648, A65
Chandar R., Leitherer C., Tremonti C. A., 2004, ApJ, 604, 153
Chen Y., Bressan A., Girardi L., Marigo P., Kong X., Lanza A., 2015, MNRAS, 452, 1068
Chisholm J., Rigby J. R., Bayliss M., Berg D. A., Dahle H., Gladders M., Sharon K., 2019, ApJ, 882, 182
Crowther P. A., 2019, Galaxies, 7, 88
Crowther P. A., 2022, preprint (arXiv:2207.08690)
Crowther P. A., Dessart L., 1998, MNRAS, 296, 622
Crowther P. A., Smith L. J., 1997, A&A, 320, 500
Crowther P. A., Walborn N. R., 2011, MNRAS, 416, 1311
Crowther P. A., Schnurr O., Hirschi R., Yusof N., Parker R. J., Goodwin S. P., Kassim H. A., 2010, MNRAS, 408, 731
Crowther P. A. et al., 2016, MNRAS, 458, 624
Crowther P. A., Castro N., Evans C. J., Vink J. S., Melnick J., Selman F., 2017, The Messenger, 170, 40
Crowther P. A., Broos P. S., Townsley L. K., Pollock A. M. T., Tehrani K. A., Gagné M., 2022, MNRAS, 515, 4130
Crowther P. A., Rate G., Bestenlehner J. M., 2023, MNRAS, 521, 585
Curti M., Cresci G., Mannucci F., Marconi A., Maiolino R., Esposito S., 2017, MNRAS, 465, 1384
Curtis-Lake E. et al., 2023, Nature Astron., 7, 622

Downloaded from https://academic.oup.com/mnras/article/527/3/9023/7455889 by guest on 16 February 2024

da Silva R. L., Fumagalli M., Krumholz M. R., 2014, MNRAS, 444, 3275
de Koter A., Heap S. R., Hubeny I., 1997, ApJ, 477, 792
de Koter A., Heap S. R., Hubeny I., 1998, ApJ, 509, 879
De Marchi G., Panagia N., 2014, MNRAS, 445, 93
De Marchi G. et al., 2011, ApJ, 739, 27
Doran E. I. et al., 2013, A&A, 558, A134
Easeman B., Schady P., Wuyts S., Yates R., 2024, MNRAS, 527 5484
Eggenberger P. et al., 2021, A&A, 652, A137
Ekström S. et al., 2012, A&A, 537, A146
Eldridge J. J., Stanway E. R., Xiao L., McClelland L. A. S., Taylor G., Ng M., Greis S. M. L., Bray J. C., 2017, Publ. Astron. Soc. Aust., 34, e058
Evans C. J., Lennon D. J., Smartt S. J., Trundle C., 2006, A&A, 456, 623
Evans C. J. et al., 2011, A&A, 530, A108
Evans C. J. et al., 2015, A&A, 574, A13
Fahrion K., De Marchi G., 2023, preprint (arXiv:2311.06336)
Feast M. W., Thackeray A. D., Wesselink A. J., 1960, MNRAS, 121, 337
Fitzpatrick E. L., Savage B. D., 1984, ApJ, 279, 578
Georgy C. et al., 2013, A&A, 558, A103
Gräfener G., Koesterke L., Hamann W. R., 2002, A&A, 387, 244
Hamann W. R. et al., 2019, A&A, 625, A57
Heap S. R., Ebbets D., Malumuth E., 1992, in European Southern Observatory Conference and Workshop Proceedings. p. 347 44 Garching: European Southern Observatory
Hénault-Brunet V. et al., 2012, A&A, 546, A73
Hillier D. J., Miller D. L., 1998, ApJ, 496, 407
Howarth I. D., 1983, MNRAS, 203, 301
Howarth I. D., Murray J., Mills D., Berry D. S., 2004, Starlink User Note, 50
Hunter D. A., Shaya E. J., Holtzman J. A., Light R. M., O'Neil Earl J. J., Lynds R., 1995, ApJ, 448, 179
Izotov Y. I., Schaerer D., Thuan T. X., Worseck G., Guseva N. G., Orlitová I., Verhamme A., 2016, MNRAS, 461, 3683
James B. L., Aloisi A., Heckman T., Sohn S. T., Wolfe M. A., 2014, ApJ, 795, 109
Johnson T. L. et al., 2017, ApJ, 843, L21
Kalari V. M., Horch E. P., Salinas R., Vink J. S., Andersen M., Bestenlehner J. M., Rubio M., 2022, ApJ, 935, 162
Keenan F. P., Aller L. H., Ryans R. S. I., Hyung S., 2001, Proc. Natl. Acad. Sci., 98, 9476
Kennicutt R. C., Jr, 1998, ARA&A, 36, 189
Kennicutt R. C. , Jr, Bresolin F., Bomans D. J., Bothun G. D., Thompson I. B., 1995, AJ, 109, 594
Kennicutt R. C. , Jr et al., 2003, PASP, 115, 928
Kewley L. J., Dopita M. A., 2002, ApJS, 142, 35
Kollmeier J. A. et al., 2017, preprint (arXiv:1711.03234)
Kroupa P., 2008, in Knapen J. H., Mahoney T. J., Vazdekis A., eds, Astronomical Society of the Pacific Conference Series 390, Pathways Through an Eclectic Universe. Astronomical Society of the Pacific, San Francisco:, p. 3
Krumholz M. R., Fumagalli M., da Silva R. L., Rendahl T., Parra J., 2015, MNRAS, 452, 1447
Lanz T., Hubeny I., 2007, ApJS, 169, 83
Leitherer C. et al., 1999, ApJS, 123, 3
Leitherer C., Ortiz Otálvaro P. A., Bresolin F., Kudritzki R.-P., Lo Faro B., Pauldrach A. W. A., Pettini M., Rix S. A., 2010, ApJS, 189, 309
Leitherer C., Ekström S., Meynet G., Schaerer D., Agienko K. B., Levesque E. M., 2014, ApJS, 212, 14
Leitherer C., Byler N., Lee J. C., Levesque E. M., 2018, ApJ, 865, 55
Maiolino R., Mannucci F., 2019, A&AR, 27, 3
Maíz Apellániz J. et al., 2014, A&A, 564, A63
Marino R. A. et al., 2013, A&A, 559, A114
Martins F., Palacios A., 2022, A&A, 659, A163
Martins F., Schaerer D., Marques-Chaves R., Upadhyaya A., 2023, A&A, 678, A159
Massey P., Hunter D. A., 1998, ApJ, 493, 180
Massey P., Parker J. W., Garmany C. D., 1989, AJ, 98, 1305
Massey P., Penny L. R., Vukovich J., 2002, ApJ, 565, 982
Massey P., Puls J., Pauldrach A. W. A., Bresolin F., Kudritzki R. P., Simon T., 2005, ApJ, 627, 477
Massey P., Morrell N. I., Neugent K. F., Penny L. R., DeGioia-Eastwood K., Gies D. R., 2012, ApJ, 748, 96
Melnick J., 1985, A&A, 153, 235
Meynet G., Maeder A., Schaller G., Schaerer D., Charbonnel C., 1994, A&AS, 103, 97
Micheva G., Oey M. S., Jaskot A. E., James B. L., 2017, ApJ, 845, 165
Mokiem M. R. et al., 2007, A&A, 473, 603
Orozco-Duarte R. et al., 2022, MNRAS, 509, 522
Pagel B. E. J., Edmunds M. G., Fosbury R. A. E., Webster B. L., 1978, MNRAS, 184, 569
Parker J. W., 1993, AJ, 106, 560
Pauldrach A. W. A., Hoffmann T. L., Lennon M., 2001, A&A, 375, 161
Peimbert A., 2003, ApJ, 584, 735
Pellegrini E. W., Baldwin J. A., Ferland G. J., 2010, ApJS, 191, 160
Pellegrini E. W., Baldwin J. A., Ferland G. J., 2011, ApJ, 738, 34
Plat A., Charlot S., Bruzual G., Feltre A., Vidal-García A., Morisset C., Chevallard J., Todt H., 2019, MNRAS, 490, 978
Prinja R. K., Crowther P. A., 1998, MNRAS, 300, 828
Ramírez-Agudelo O. H. et al., 2017, A&A, 600, A81
Rickard M. J. et al., 2022, A&A, 666, A189
Rivera-Thorsen T. E. et al., 2017, A&A, 608, L4
Rivera-Thorsen T. E. et al., 2019, Science, 366, 738
Robert C., Leitherer C., Heckman T. M., 1993, ApJ, 418, 749
Roman-Duval J. et al., 2020, Res. Notes Am. Astron. Soc., 4, 205
Russell S. C., Dopita M. A., 1990, ApJS, 74, 93
Sabbi E. et al., 2013, AJ, 146, 53
Sabbi E. et al., 2016, ApJS, 222, 11
Sabín-Sanjulián C. et al., 2017, A&A, 601, A79
Sana H. et al., 2013, A&A, 550, A107
Sánchez S. F. et al., 2022, ApJS, 262, 36
Saxena A. et al., 2020, A&A, 636, A47
Schaerer D., Vacca W. D., 1998, ApJ, 497, 618
Schaller G., Schaerer D., Meynet G., Maeder A., 1992, A&AS, 96, 269
Schneider F. R. N. et al., 2018a, Science, 359, 69
Schneider F. R. N. et al., 2018b, A&A, 618, A73
Selman F., Melnick J., Bosch G., Terlevich R., 1999, A&A, 341, 98
Shenar T. et al., 2017, A&A, 598, A85
Shenar T. et al., 2019, A&A, 627, A151
Shenar T. et al., 2022, A&A, 665, A148
Sidoli F., Smith L. J., Crowther P. A., 2006, MNRAS, 370, 799
Sirressi M. et al., 2022, AJ, 164, 208
Smith L. J., Norris R. P. F., Crowther P. A., 2002, MNRAS, 337, 1309
Smith L. J., Crowther P. A., Calzetti D., Sidoli F., 2016, ApJ, 823, 38
Smith L. J. et al., 2023, ApJ, 958, 194
Stanway E. R., Eldridge J. J., 2018, MNRAS, 479, 75
Steidel C. C., Strom A. L., Pettini M., Rudie G. C., Reddy N. A., Trainor R. F., 2016, ApJ, 826, 159
Tehrani K. A., Crowther P. A., Bestenlehner J. M., Littlefair S. P., Pollock A. M. T., Parker R. J., Schnurr O., 2019, MNRAS, 484, 2692
Vacca W. D., Robert C., Leitherer C., Conti P. S., 1995, ApJ, 444, 647
Vanzella E. et al., 2022, A&A, 659, A2
Vermeij R., van der Hulst J. M., 2002, A&A, 391, 1081
Verro K. et al., 2022, A&A, 661, A50
Vink J. S., Muijres L. E., Anthonisse B., de Koter A., Gräfener G., Langer N., 2011, A&A, 531, A132
Vink J. S. et al., 2023, A&A, 675, A154
Walborn N. R., Blades J. C., 1997, ApJS, 112, 457
Walborn N. R. et al., 2014, A&A, 564, A40
Welty D. E., Xue R., Wong T., 2012, ApJ, 745, 173
Wofford A., Leitherer C., Salzer J., 2013, ApJ, 765, 118
Wofford A., Leitherer C., Chandar R., Bouret J.-C., 2014, ApJ, 781, 122
Wofford A. et al., 2023, MNRAS, 523, 3949
Wong T. et al., 2022, ApJ, 932, 47

Downloaded from https://academic.oup.com/mnras/article/527/3/9023/7455889 by guest on 16 February 2024

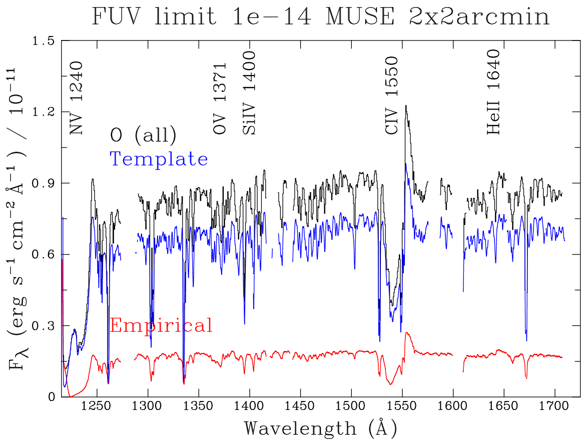

Figure A1. Cumulative O-type far-UV spectrum of the central region of NGC 2070 (black) based on empirical data of 34 individual stars (red) and 159 LMC template stars (blue). Gaps in spectra arise from incomplete spectral coverage (e.g. COS G130M + G160M).

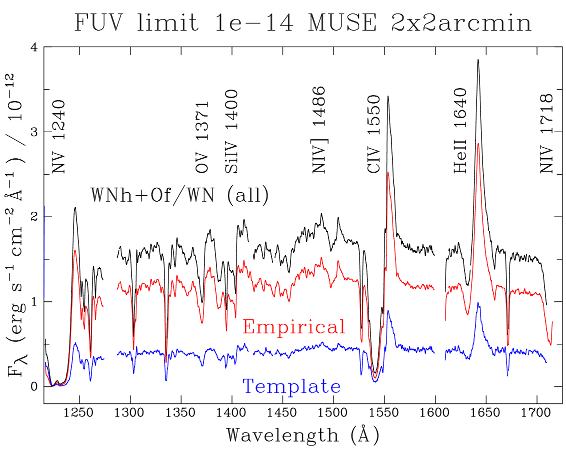

Figure A2. Cumulative WNh+Of/WN far-UV spectrum of the central region of NGC 2070 (black) based on empirical data of 7 individual stars (red) and 5 LMC template stars (blue). Gaps in spectra arise from incomplete spectral coverage (e.g. COS G130M + G160M).

APPENDIX A: TEMPLATE UV SPECTRA

The NGC 2070 far-UV spectrum has been constructed from a combination of empirical spectra (of individual stars) and use of template OB stars (Table A1) and Of/WN and WR stars (Table A2 for the remainder, primarily drawn from Data Release 6 (DR6)

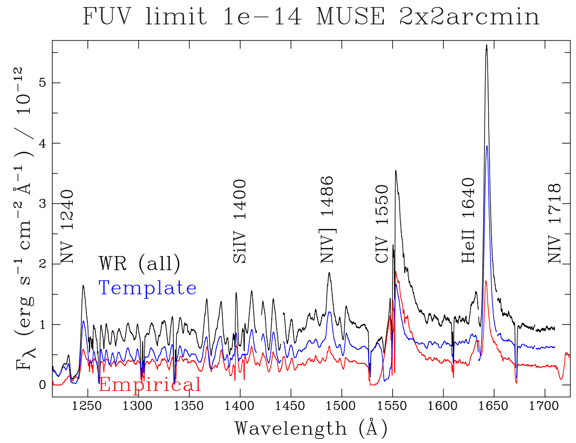

Figure A3. Cumulative WR far-UV spectrum of the central region of NGC 2070 (black) based on empirical data of R140a1 (red, WN + WC) and 5 LMC template stars (blue, 4 WN, 1 WC).

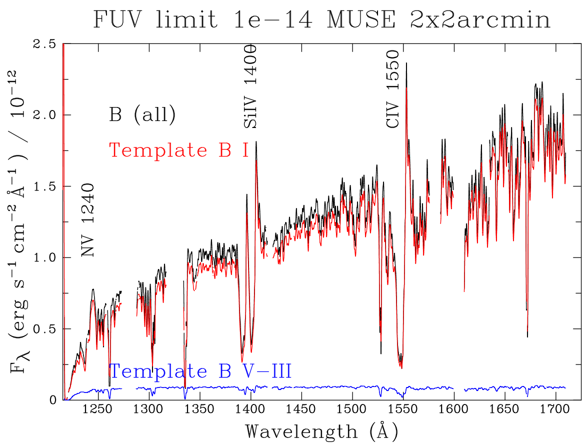

Figure A4. Cumulative B-type far-UV spectrum of the central region of NGC 2070 (black) based on LMC templates for 10 supergiants (red) and 6 non-supergiants (blue). Gaps in spectra arise from incomplete spectral coverage (e.g. COS G130M + G160M).

of the ULLYSES survey (Roman-Duval et al. 2020). Figs A1–A4 present cumulative far-UV spectra for O, Of/WN, WR, and B stars, respectively, including breakdowns between empirical data sets and templates (separated into supergiants and non-supergiants for B stars).

Downloaded from https://academic.oup.com/mnras/article/527/3/9023/7455889 by guest on 16 February 2024

Table A1. LMC template UV spectra of normal OB stars from HST ULLYSES survey (Roman-Duval et al. 2020). COS gratings G130M + G160M are abbreviated as G1#0M.

Template	— Dwarf — Star (Sp Type)	Instrument/Grating	— Giant — Star (Sp Type)	Instrument/Grating	— Supergiant — Star (Sp Type)	Instrument/Grating
O2	BI 237 (O2 V)	COS G1#0M	VFTS 72 (O2 V–III)	COS G1#0M	Mk 42 (O2 If∗)	STIS/E140M
O2.5	VFTS 169 (O2.5 V)	COS G1#0M	N11 ELS 26 (O2.5 III)	COS G1#0M	...	...
O3	N11 ELS 60 (O3 V)	COS G1#0M	VFTS 267 (O3 III-I)	COS G1#0M	VFTS 180 (O3 If∗)	STIS E140M
O3.5	VFTS 404 (O3.5: V:)	COS G1#0M	...	...	...	...
O4	W61 28-5 (O4 V)	COS G1#0M	Sk –67° 69 (O4 III)	STIS E140M	Sk –67° 166 (O4 I)	STIS E140M
O4.5	Sk –70° 60 (O4–5 V)	STIS E140M	...	...	...	...
O5	PGMW 3120 (O5.5 V)	STIS E140M	N11 ELS 38 (O5 III)	COS G1#0M	[ST92] 4-18 (O5 If)	COS G1#0M
O6	PGMW 3070 (O6 V)	STIS E140M	Sk –71° 19 (O6 III)	COS G1#0M	Sk –67° 111 (O6 Iafpv)	STIS E140M
O6.5	...	...	Sk –71° 50 (O6.5 III)	STIS E140M	...	...
O7	Sk –67° 118 (O7 V)	STIS E140M	BI 272 (O7 II)	STIS E140M	Sk –69° 83 (O7.5 Iaf)	STIS E140M
O8	BI 184 (O8 V)	COS G1#0M	Sk –67° 101 (O8 II)	STIS E140M	PGMW 1363 (O8.5 Iaf)	STIS E140M
O9	VFTS 66 (O9 V)	COS G1#0M	Sk –71° 8 (O9 II)	STIS E140M	Sk –67° 107 (O9 Ib)	STIS E140M
O9.5	...	...	Sk –66° 17 (OC9.5 II)	COS G1#0M	Sk –67° 5 (O9.7 Ib)	STIS E140M
B0	HV 5622 (B0 V)	COS G1#0M	Sk –70° 79 (B0 III)	STIS E140M	Sk –68° 52 (B0 Ia)	STIS E140M
B0.5	Sk –67° 216 (B0.5 V)	STIS E140M	...	...	Sk –68° 155 (B0.5 I)	COS G1#0M
B0.7	...	...	...	...	Sk –68° 140 (B0.7 Ib-Iab)	COS G1#0M
B1	Sk –65° 2 (B1 V)	STIS E140M	Sk –71° 35 (B1 II)	COS G1#0M	Sk –66° 35 (BC1 Ia)	COS G1#0M
B1.5	...	...	...	...	Sk –67° 14 (B1.5 Ia)	STIS E140M
B2	...	...	...	...	Sk –68° 26 (BC2 Ia)	COS G1#0M
B9	...	...	...	...	Sk –67° 207 (B9 Ia)	COS G1#0M

Table A2. LMC template UV spectra of normal Of/WN and WR stars from HST ULLYSES survey (Roman-Duval et al. 2020) except where noted.

Template	Star (Sp Type)	Instrument/Grating
O2 If/WN5	Sk -67° 22 (O2 If/WN5)	STIS/E140M
O2.5 If/WN6	Mk 39 (O2.5 If/WN6)	COS G130M + G160M
O3.5 If/WN7	Mk 51 (O3.5 If/WN7)	COS G140L[c]
O4 If/WN8	R136b (O4 If/WN8)	GHRS G140L[a]
WN5h	R136a3 (WN5h)	GHRS G140L[b]
WN6	Sk -71° 21 (WN6h)	STIS E140M
WN7–8	VFTS 108 (WN7h)	COS G140L[c]
WC4	Sk -69° 191 (WC4)	STIS E140M

a: de Koter, Heap & Hubeny (1998), b: de Koter, Heap & Hubeny (1997); c: GO 15629 (Mahy)

APPENDIX B: CENSUS OF FAR-UV BRIGHTEST SOURCES OF NGC 2070

Table B1 lists stars of known spectral type within the MUSE footprint, sorted by far-UV flux, based on a calibration of F275W or F336W photometry drawn from HTTP (Sabbi et al. 2013, 2016). HSH95-17 is included since it lies within R136 GHRS/G140L 2 × 2 arcsec^2 region and is considered to be an early O star (Kalari et al. 2022), although a few other sources exceeding $F_{1500} \geq 10^{-14}$ erg s^{-1} cm^{-2} Å^{-1} have been excluded since their spectral types are unknown. These include HSH95-76 [P 870, $m_{\rm F275W}$ = 13.57 mag, Sabbi et al. (2016)], SMB 136 [$m_{\rm 275W}$ = 13.88 mag, Sabbi et al. (2016)], HSH95-87 [$m_{\rm F336W}$ = 14.27 mag, Sabbi et al. (2016)], HSH95 120 [$m_{\rm F275W}$ = 14.55 mag, Sabbi et al. (2016)], HSH95-139 [$m_{\rm F336W}$ = 14.80 mag, Hunter et al. (1995)], and HSH95-129 [$m_{\rm F336W}$ = 14.97 mag, Hunter et al. (1995)].

Table B2 lists stars of known spectral type beyond the MUSE footprint but within the 3 × 3 arcmin^2 region sampled with *IUE*/SWP (Vacca et al. 1995), sorted by far-UV flux, based on a calibration of F275W or F336W photometry drawn from HTTP (Sabbi et al. 2013, 2016). Bright sources lacking spectral types include SMB-183 [$m_{\rm 275W}$ = 14.11 mag, Sabbi et al. (2016)], SMB-196 [$m_{\rm 275W}$ = 14.27 mag, Sabbi et al. (2016)], and SMB-245 [$m_{\rm 275W}$ = 14.67 mag, Sabbi et al. (2016)].

Downloaded from https://academic.oup.com/mnras/article/527/3/9023/7455889 by guest on 16 February 2024

Table B1. Stars within the NGC 2070 MUSE field of view, sorted by far-UV flux (F_{1500} units of erg s^{-1} cm^{-2} Å^{-1}), either measured from spectroscopy or estimated from photometry, primarily drawn from HTTP (Sabbi et al. 2013, 2016), the latter indicated in parentheses. Catalogues include R (Feast, Thackeray & Wesselink 1960), Mk (Melnick 1985), P (Parker 1993), HSH (Hunter et al. 1995), SMB (Selman et al. 1999), VFTS (Evans et al. 2011), and CCE (Castro et al. 2018). Spectra used in our integrated far-UV spectrum of NGC 2070 are of individual sources or templates with the exception of GHRS/G140L spectroscopy of the central 2 × 2 arcsec of R136a (indicated with ‡) while several templates are adjusted to measured STIS/G140L flux levels from Massey et al. (2005, indicated with †). Further details of far-UV templates are provided in Tables A1–A2. Sources considered to be VMSs (≥100 M$_\odot$) from spectroscopy analyses (Bestenlehner et al. 2014; Tehrani et al. 2019; Brands et al. 2022) are indicated with ✓. COS gratings G130M + G160M are abbreviated as G1#0M.

R	Mk	P	HSH	SMB	VFTS	CCE	SpT	Ref	HTTP	m_{275W} mag	m_{F336W} mag	m_{F555W} mag	Ref	F_{1500} 10^{-13}	Spectrum (Template)	Ref	VMS
140a	···	877	···	6	507	3191	WC4+WN6 +	Do13	053841.601-690513.43	10.97	11.28	12.20	S	3.72	STIS/E140M	1	···
136a1	···	···	3	7	···	···	WN5h	CD98	···	···	11.20	12.28	D	(3.32)	GHRS/G140L‡	4	✓
140b	···	880	···	8	509	3174	WN5(h) + O	Ev11	053841.613-690515.17	11.09	11.43	12.47	S	(3.04)	(WN6)	···	···
···	42	922	2	10	···	2102	O2 If	CW11	053842.104-690555.29	11.08	11.51	12.82	S	3.01	STIS/E140M	3	✓
136a2	···	···	5	···	···	···	WN5h	CD98	···	···	11.33	12.34	D	(2.93)	GHRS/G140L‡	4	✓
···	39	767	7	14	482	2003	O2.5 If/WN6 +	Cr22	053840.214-690559.86	11.38	11.66	12.95	S	2.74	COS/G1#0M	3	✓
142	···	987	1	3	533	2912	B1.5 Ia$^+$	Ev15	053842.738-690542.57	10.84	11.13	11.79	S	(2.50)	(B1.5 I)	···	···
134	···	786	4	···	1001	1978	WN6(h)	CS97	053840.539-690557.18	11.45	11.62	12.70	S	(2.18)	(WN6)	···	···
137	···	548	···	5	431	2889	B1.5 Ia	Ev15	053836.959-690507.84	11.04	11.30	12.08	S	(2.08)	(B1.5 I)	···	···
···	25	871	···	19	506	2395	ON2 V	Wa14	053841.545-690519.43	11.74	12.01	13.32	S	2.04	COS/G1#0M	3	✓
141	···	1253	···	9	590	2190	B0.7 Iab	Ev15	053845.579-690547.80	11.42	11.60	12.58	S	(1.92)	(B0.7 I)	···	···
136a3	···	···	6	···	···	···	WN5h	CD98	···	···	11.82	12.97	D	(1.87)	GHRS/G140L‡	4	✓
···	30	1018	15	24	542	2999	O2 If/WN5	CW11	053843.080-690546.86	11.91	12.22	13.48	S	1.85	COS/G1#0M	3	···
···	12	1257	···	11	591	1279	B0.2 Ia	Ev15	053845.687-690622.49	···	11.68	12.56	S	(1.80)	(B0 I)	···	···
···	35	1029	12	23	545	1474	O2 If/WN5	CW11	053843.202-690614.44	11.93	12.23	13.46	S	(1.40)	(O2 I/WN5)	···	✓
···	32	1130	13	21	1034	3043	O7.5 II	WB97	053844.192-690547.06	11.96	12.23	13.40	S	(1.37)	(O8 III)	···	···
···	34	1134	8	17	···	1766	WN5h + WN5h	Te19	053844.252-690605.93	12.04	12.11	13.15	S	(1.28)	(WN5)	···	✓
138	···	499	···	4	424	···	B9 I + p	Ev15	053836.132-690558.01	···	11.50	11.79	S	(1.25)	(B9 I)	···	···
···	37Wa	917	11	25	1021	1349	O4 If$^+$	MH98	053842.072-690614.32	12.16	12.35	13.36	S	(1.14)	(O4 I)	···	✓
···	11	1500	···	15	641	762	B0.5: I	Ev15	053849.723-690642.95	···	12.19	13.18	S	(1.13)	(B0.5 I)	···	···
···	35Sa	1036	23	37	1028	1423	O4–5 V	WB97	053843.263-690616.51	12.18	12.53	13.85	S	(1.12)	(O4.5 V)	···	···
···	···	1080	25	39	1031	2186	O3–4 V	Bo99	053843.684-690547.89	12.20	12.56	14.23	S	(1.10)	(O3 V)	···	···
···	13	1311	···	40	599	1433	O3 III	Wa14	053846.177-690617.39	12.28	12.63	13.85	S	(1.02)	(O3 III)	···	···
···	26	1150	···	32	562	2819	O4 III	WB97	053844.406-690536.22	12.28	12.46	13.70	S	(1.02)	(O4 III)	···	···
136a5	···	···	20	···	···	···	O2 If	Cr16	···	···	12.49	13.71	D	(1.01)	GHRS/G140L‡	4	✓
136c	···	998	10	27	1025	1737	WN5h + ?	Cr10	···	···	12.54	13.43	D	(0.97)	(WN5)	···	✓
···	47	607	···	29	440	2417	O6–6.5 III	Wa14	053837.729-690521.03	12.15	12.44	13.69	S	0.96	STIS/E140M	2	···
···	33Na	1140	16	33	···	1943	OC2.5 If + O4 V	Br22	053844.329-690554.66	12.37	12.55	13.64	S	(0.94)	(O3 I)	···	···
···	54	488	···	16	420	1689	B0.5 Ia	Ev15	053835.941-690609.23	12.20	12.26	13.10	S	(0.93)	(B0.5 I)	···	···
···	27	850	···	38	502	2653	O9.7 II	Wa14	053841.271-690532.44	12.39	12.67	13.82	S	(0.92)	(O9.5 III)	···	···
···	···	1014	···	41	···	3062	O8:	Ca21	053843.030-690540.44	12.43	12.57	13.60	S	(0.89)	(O8 III)	···	···
136a7	···	···	24	20	···	···	O3 III(f*)	Be20	···	···	12.64	13.97	S	(0.88)	GHRS/G140L‡	4	✓
···	···	860	28	53	···	1912	O3 V	MH98	053841.490-690556.90	12.45	12.80	14.04	S	(0.87)	(O3 V)	···	···
···	···	1231	···	31	585	2193	O7 V	Wa14	053845.279-690546.53	···	12.66	13.78	S	(0.87)	(O7 V)	···	···
136b	···	985	9	18	···	1669	O4 If/WN8	Cr16	···	···	12.27	13.24	D	0.86	GHRS/G140L	5	✓
···	37a	949	14	28	1022	1442	O3.5 If/WN7	CW11	053842.397-690615.08	12.33	12.48	13.52	S	0.82†	(O3.5 If/WN7)	6	✓
···	24	1260	···	47	···	2760	O3 V	WB97	053845.687-690539.02	12.53	12.73	13.96	S	(0.81)	(O3 V)	···	···
140c	···	908	···	55	519	3112	O3–4((f)) + OB	Wa14	053841.934-690513.02	12.53	12.81	14.18	S	(0.81)	(O3.5 V)	···	···
···	···	863	29	56	1014	1956:	O3 V	MH98	053841.507-690600.92	12.55	12.90	14.18	S	(0.80)	(O3 V)	···	···
···	33Sa	1120	18	44	···	2177	O3 III	Ma15	053844.123-690556.63	12.48	12.76	13.81	S	0.79†	(O3 III)	6	···
···	50	643	···	34	450	1293	O9.7 III: + O7::	Wa14	053838.476-690621.96	12.57	12.75	13.69	S	(0.78)	(O9.5 III)	···	···

Downloaded from https://academic.oup.com/mnras/article/527/3/9023/7455889 by guest on 16 February 2024

Table B1 – *continued*

R	Mk	P	HSH	SMB	VFTS	CCE	SpT	Ref	HTTP	m_{275W} mag	m_{F336W} mag	m_{F555W} mag	Ref	F_{1500} 10^{-13}	Spectrum (Template)	Ref	VMS
136a4	···	···	21	···	···	···	O3 V	Be20	···	···	12.81	13.96	H	(0.75)	GHRS/G140L‡	4	✓
···	···	923	33	60	···	1793	O3 V	Ma05	053842.119-690600.73	···	13.09	14.33	S	0.75†	(O3 V)	6	···
136a6 #1	···	···	19	···	···	···	O2 I(n)f∗p + ?	Be20	···	···	12.86	13.92	H	(0.72)	GHRS/G140L‡	4	···
···	49	691	···	30	···	1261	WN6(h)	CS97	053839.143-690621.24	12.66	12.62	13.41	S	(0.71)	(WN6)	···	···
136a6 #2	···	···	26	···	···	···	O2 I(n)f∗p + ?	Be20	···	···	12.89	14.19	H	(0.70)	GHRS/G140L‡	4	···
···	···	912	38	70	1019	1608	O3 V + O6 V	Ma02	053842.004-690607.56	12.72	13.02	14.30	S	(0.68)	(O3 V)	···	···
···	6	1563	···	61	656	1979	O7.5 IIIp	Wa14	053851.200-690559.28	12.73	13.11	14.36	S	(0.68)	(O7 III)	···	···
···	8	1531	···	58	648	2780	O5.5 IV	Wa14	053850.400-690538.17	12.73	12.96	14.23	S	(0.67)	(O5.5 V)	···	···
···	38	930	···	45	525	1184	B0 Ia	Wa14	053842.209-690625.56	12.55	12.79	13.83	S	(0.67)	(B0 I)	···	···
136a8	···	···	27	···	···	···	O2–3 V	Cr16	···	···	12.93	14.22	H	(0.67)	GHRS/G140L‡	4	···
···	···	···	17	···	···	···	O	Ka22	···	···	13.00	13.78	H	(0.63)	GHRS/G140L‡	4	···
···	···	1273	···	59	···	1223	O7:	Ca21	053845.842-690620.83	12.82	13.05	14.05	S	(0.62)	(O7 III)	···	···
···	···	···	30	···	···	···	O6.5 Vz	Be20	···	···	13.02	14.21	D	(0.62)	GHRS/G140L‡	4	···
···	···	···	31	35	···	···	O2 V	Be20	053842.471-690604.53	···	12.89	14.05	S	0.61†	(O2 V)	···	···
···	···	713	···	72	···	2245	O5 V	Bo99	053839.478-690510.36	12.85	13.20	14.60	S	(0.60)	(O4.5 V)	···	···
···	···	···	36	···	···	···	O2 If	Be20	···	···	13.06	14.41	S	(0.59)	(O2 I)	···	✓
···	···	···	35	···	···	···	O3 V	Be20	···	···	13.12	14.43	D	0.55†	GHRS/G140L‡	4	···
···	···	975	···	71	···	2748	O6–7 V	Bo99	053842.616-690536.74	12.93	13.18	14.50	S	(0.56)	(O6 V)	···	···
···	15	1312	···	43	···	2165	O7 V	WB97	053846.158-690551.37	···	13.14	14.13	S	(0.55)	(O7 V)	···	···
···	···	1113	53	78	1032	2977	O8 III	Le21	053844.063-690544.82	12.97	13.32	14.63	S	(0.54)	(O8 III)	···	···
140d	···	···	···	81	497	2231	O3.5 Vz + OB	Wa14	053841.126-690513.17	12.97	13.28	14.65	S	(0.54)	(O3.5 V)	···	···
···	···	···	42	···	···	···	O3 V + O3 V	Ma02	053842.119-690600.73	12.98	13.34	14.71	S,D	(0.54)	(O3 V)	···	···
···	···	···	75	···	···	···	O6 V	Be20	053842.178-690601.90	13.01	13.86	15.08	S,D	(0.52)	(O6 V)	···	···
···	···	288	···	84	385	2451	O4–5V	Wa14	O53832.293-690523.85	13.22	13.38	14.65	S	0.51	COS/G140L	2	···
···	33Nb	1152	32	66	···	1896	O6.5 V	Be20	053844.467-690555.50	13.03	13.28	14.36	S	(0.51)	(O6 V)	···	···
···	···	1034	61	85	1027	2987	O5 V	Le21	053843.195-690542.61	13.05	13.38	14.68	S	(0.50)	(O4.5 V)	···	···
···	···	···	39	···	1005	···	O3 V + O5.5 V	Ma02	···	···	13.26	14.50	D	(0.50)	(O3 V)	···	···
···	53	···	···	51	427	389	WN8(h)	Ev11	053836.407-690657.48	···	13.27	13.77	S	(0.49)	(WN7–8)	···	···
···	35N	1013	41	76	1026	1494	O3 III(f∗)	MH98	053843.075-690611.28	···	13.29	13.97	S,D	(0.48)	(O3 III)	···	···
···	···	1042	56	87	1029	2128	O3.5I + OB	Wa14	053843.343-690547.55	13.10	13.39	14.71	S,D	(0.48)	(O3 I)	···	···
···	···	···	40	···	···	···	O3 V	Be20	···	···	13.30	14.56	D	(0.48)	(O3 V)	···	···
···	···	1195	43	83	···	2112	O3 V	MH98	053844.950-690554.11	13.12	13.37	14.57	S	(0.47)	(O3 V)	···	···
···	···	1123	···	74	1033	2913	O7 III	Le21	053844.172-690542.17	13.13	13.42	14.53	S	(0.46)	(O7 III)	···	···
···	···	885	···	68	512	1199	O2 V-III	Wa14	053841.734-690625.01	13.15	13.30	14.34	S	(0.46)	(O2 V)	···	···
···	51	666	···	50	457	603	O3.5 If/WN7	CW11	053838.838-690649.49	···	12.98	13.81	S	0.45	COS/G140L	2	✓
···	···	724	···	75	···	1274	O7 III	Bo99	053839.692-690624.01	13.17	13.37	14.41	S	(0.45)	(O7 III)	···	···
···	14S	1350	···	64	608	1827	O4 III	Wa14	053846.785-690603.10	13.01	13.19	14.29	S	0.43	COS/G140L	2	···
···	···	723	···	92	···	2570	O5:	Ca21	053839.638-690526.37	13.21	13.53	14.77	S	(0.43)	(O5 III)	···	···
···	36	706	···	86	468	1749	O2 V	Wa14	053839.369-690606.49	13.21	13.39	14.58	S	(0.43)	(O2 V)	···	···
···	···	812	51	89	···	···	O3 V	MH98	053840.895-690555.93	13.23	13.48	14.70	S	(0.43)	(O3 V)	···	···

Downloaded from https://academic.oup.com/mnras/article/527/3/9023/7455889 by guest on 16 February 2024

Table B1 – *continued*

R	Mk	P	HSH	SMB	VFTS	CCE	SpT	Ref	HTTP	$m_{275\mathrm{W}}$ mag	m_{F336W} mag	m_{F555W} mag	Ref	F_{1500} 10^{-13}	Spectrum (Template)	Ref	VMS
···	27E	858	···	100	503	···	O9 III	Wa14	053841.367-690532.44	13.23	13.57	14.87	S,D	(0.43)	(O9 III)	···	···
···	···	1267	···	90	···	2911	O7: V	Pa93	053845.757-690540.82	13.24	13.52	14.72	S	(0.42)	(O7 V)	···	···
···	28	805	···	80	···	2447	O5–6 V	Bo99	053840.798-690525.10	13.24	13.40	14.61	S	(0.42)	(O5.5 V)	···	···
···	···	787	···	103	···	2233	O9–B0 V	Bo99	053850.435-690534.56	13.25	13.60	14.98	S	(0.42)	(O9 V)	···	···
···	4	1607	···	65	664	774	O7 II	Wa14	053852.724-690643.13	···	13.37	14.38	S	0.41	COS/G140L	2	···
···	···	···	52	···	···	···	O3–4 Vz	Be20	···	···	13.46	14.72	D	(0.41)	GHRS/G140L‡	4	···
···	···	···	45	···	···	···	O4: Vz	Be20	···	···	13.48	13.65	D	(0.40)	(O4 V)	···	···
···	···	900	37	77	1018	1459	O2–4.5	He12	053841.874-690612.52	13.29	13.42	14.49	D	(0.40)	(O3 III)	···	···
···	···	···	49	···	···	···	O3 V	Be20	···	···	13.49	14.75	D	(0.40)	(O3 V)	···	···
···	···	···	50	···	···	···	O3–4 V	Be20	···	···	13.51	14.65	D	(0.39)	GHRS/G140L‡	4	···
···	···	···	55	···	···	···	O2 Vz	Be20	···	···	13.52	14.74	D	(0.39)	(O2 V)	···	···
···	5	1552	···	54	652	1405	B2 Ip + O9III:	Wa14	053851.043-690620.40	···	13.06	14.15	S	(0.39)	(B2 I)	···	···
···	···	···	46	···	···	···	O2–3 III	Be20	···	···	13.53	14.56	S	(0.39)	(O2.5 III)	···	···
···	···	506	···	82	···	1632	O8:	Ca21	053836.237-690608.42	13.35	13.52	14.55	S	(0.38)	(O8 III)	···	···
···	14N	1317	···	91	601	1890	O5–6 V	Wa14	053846.280-690559.32	13.36	13.56	14.68	S	(0.38)	(O5.5 V)	···	···
···	7	1553	···	94	651	2057	O7 V	Wa14	053851.029-690554.70	13.36	13.59	14.74	S	(0.38)	(O7 V)	···	···
···	···	···	47	111	···	···	O2 V	Be20	053842.630-690601.92	13.39	13.66	14.72	S	(0.37)	(O2 V)	···	···
···	···	···	48	···	···	···	O2–3 III	Be20	···	···	13.60	14.75	D	(0.36)	(O2.5 III)	···	···
···	···	···	58	···	···	···	O2–3 V	Be20	···	···	13.61	14.80	D	(0.36)	GHRS/G140L‡	4	···
···	···	467	···	93	416	1700	O8.5 V	Ma12	053835.570-690606.65	13.41	13.57	14.74	S	(0.36)	(O8 V)	···	···
···	···	···	···	106	583	2107	O8 V + O8.5 V	Wa14	053845.211-690548.48	13.44	13.71	14.92	S	(0.35)	(O8 V)	···	···
···	···	···	62	···	···	···	O2–3 V	Be20	···	···	13.65	14.91	D	(0.35)	GHRS/G140L‡	4	···
···	52	493	···	48	423	660	B1 Ia	Ev15	053836.053-690646.50	···	13.19	13.64	S	(0.34)	(B1 I)	···	···
···	···	1340	···	110	604	2884	O8.5 V	Wa14	053846.567-690537.10	13.47	13.71	14.95	S	(0.34)	(O8 V)	···	···
···	···	1248	···	112	···	3034	O6:	Ca21	053845.494-690543.99	13.48	13.73	15.00	S	(0.34)	(O6 III)	···	···
···	···	1614	···	118	667	1699	O6 V	Wa14	053852.832-690612.01	···	13.95	15.08	S	0.33	COS/G140L	2	···
···	···	···	86	···	···	···	O5: V	Be20	···	···	13.72	14.73	D	(0.33)	GHRS/G140L‡	4	···
···	···	827	60	95	1007	1763	O6.5 V-III	He12	053841.066-690601.89	···	13.72	14.86	S,D	(0.32)	(O6.5 III)	···	···
···	···	···	67	96	···	1857:	O6:	Ca21	053841.324-690557.59	13.52	13.86	15.09	S,D	(0.32)	(O6 III)	···	···
···	···	661	···	108	455	1572	O5:V:n	Wa14	053838.759-690613.22	13.55	13.75	15.08	S	(0.32)	(O4.5 V)	···	···
···	···	1281	···	114	···	2033	O7:	Ca21	053845.907-690550.77	13.56	13.76	14.90	S	(0.31)	(O7 III)	···	···
···	37Wb	897	44	88	1017	1374	O2 If/WN5	CW11	053841.862-690614.41	13.56	13.60	14.53	S	(0.31)	(O2 If/WN5)	···	✓
···	···	761	63	105	···	2077	O3–6 V	WB97	053840.143-690551.26	13.56	13.76	14.86	S	(0.31)	(O4.5 V)	···	···
···	·	781	72	113	···	1974	O6:	Ca21	053840.477-690553.42	13.57	13.83	14.99	S	(0.31)	(O6 III)	···	···
···	···	···	70	···	···	···	O5 Vz	Be20	···	···	13.81	14.96	D	(0.30)	GHRS/G140L‡	4	···
···	···	···	74	121	···	···	O6 V	MH98	···	···	13.82	15.11	D	(0.30)	(O6 V)	···	···
···	···	1329	···	122	···	2718	O9:	Ca21	053849.107-690547.18	13.63	13.86	15.23	S	(0.29)	(O9 III)	···	···
···	···	1023	59	99	···	1703	O3 III	MH98	053843.168-690603.65	13.63	13.73	14.76	S,D	(0.29)	(O3 III)	···	···
···	···	974	···	104	532	963	O3 V(n)z + OB	Wa14	053842.657-690635.83	···	13.85	14.81	S	(0.29)	(O3 V)	···	···
···	···	978	54	109	···	1963	O4:	Ca21	053842.679-690556.30	13.67	13.80	14.79	S	(0.28)	(O4 III)	···	···
···	···	···	71	···	···	···	O2–3 V	Be20	053842.365-690604.90	13.70	13.98	15.16	S,D	(0.28)	(O2.5 V)	···	···

Downloaded from https://academic.oup.com/mnras/article/527/3/9023/7455889 by guest on 16 February 2024

Table B1 – *continued*

R	Mk	P	HSH	SMB	VFTS	CCE	SpT	Ref	HTTP	m_{275W} mag	m_{F336W} mag	m_{F555W} mag	Ref	F_{1500} 10^{-13}	Spectrum (Template)	Ref	VMS
…	…	…	57	…	…	…	O3 III(f*)	MH98	…	…	13.90	14.80	D	(0.28)	(O3 III)	…	…
…	…	776	…	124	484	3081	O6–7 V	Wa14	053840.354-690543.79	13.71	13.94	15.09	D	(0.27)	(O6 V)	…	…
…	…	921	82	134	522	3030	O6 II-Iab + O5.5 V	Wa14	053842.082-690545.47	13.72	14.01	15.26	S	(0.27)	(O6 III)	…	…
…	…	…	77	…	…	…	O5.5 V + O5.5 V	Ma02	…	…	13.94	15.21	D	(0.27)	(O5.5 V)	…	…
…	…	1196	…	130	…	2763	O6:	Ca21	053844.958-690538.63	13.75	13.89	15.14	S	(0.26)	(O6 III)	…	…
…	…	…	80	…	…	…	O8 V	Be20	…	…	13.95	15.17	D	(0.26)	(O8 V)	…	…
…	…	973	…	129	…	2545	O8:	Ca21	053842.607-690522.21	13.75	14.05	15.25	S	(0.26)	(O8 III)	…	…
…	…	…	66	…	…	…	O2 V-III	Be20	…	…	13.95	15.06	D	(0.26)	GHRS/G140L‡	4	…
…	33Sb	1111	34	…	…	…	WC5	MH98	053844.062-690555.64	13.76	13.82	14.49	S	(0.26)	(WC4)	…	…
…	…	600	…	123	…	2946	O3–5 V	Bo99	053837.658-690542.06	…	13.96	15.04	S	(0.26)	(O4 V)	…	…
…	15S	1306	…	117	…	2053	O8 III	WB97	053846.113-690554.44	13.79	13.93	14.95	S	(0.25)	(O8 III)	…	…
…	…	…	89	…	…	…	O4 V	Cr16	…	…	13.99	14.76	D	(0.25)	GHRS/G140L‡	4	…
…	…	621	…	97	445	2981	O3–4 V + O4–7 V	Wa14	053838.026-690543.30	13.80	13.58	14.79	S	(0.25)	(O3.5 V)	…	…
…	…	…	69	…	…	…	O4–5 V	Be20	…	…	14.02	15.05	D,H	(0.25)	GHRS/G140L‡	4	…
…	…	…	65	…	…	…	O4 V	Cr16	…	…	14.03	15.18	D	(0.24)	(O4 V)	…	…
…	…	…	64	…	…	…	O4–5 V	Be20	053842.646-690601.05	13.83	13.95	14.53	S	(0.24)	(O4 V)	…	…
…	…	…	78	…	…	…	O4: V	Be20	…	…	14.04	15.26	D	(0.24)	GHRS/G140L‡	4	…
…	…	324	…	131	393	2256	O9.5(n)	Wa14	053832.992-690513.05	13.87	14.04	15.26	S	(0.24)	(O9.5 III)	…	…
…	…	977	…	139	…	2893	O6: V	Bo99	053842.636-690538.69	13.88	14.12	15.36	S	(0.23)	(O6 V)	…	…
…	…	1222	…	116	…	3180	O3–6 V	WB97	053845.150-690508.34	13.88	14.08	14.99	S	(0.23)	(O4.5 V)	…	…
…	…	…	73	…	…	…	O9.7–B0 V	Be20	…	…	14.12	15.13	D	(0.23)	GHRS/G140L‡	4	…
…	…	1594	…	125	661	2691	O6.5 V + O9.7 V	Wa14	053852.049-690533.79	13.94	14.00	15.19	S	(0.22)	(O6 V)	…	…
…	…	1295	…	137	596	1325	O7–8 V	Wa14	053846.059-690615.55	13.97	14.25	15.35	S	(0.21)	(O7 V)	…	…
…	…	884	…	143	511	1008	O5 Vz	Wa14	053841.717-690628.13	13.98	14.21	15.31	S	(0.21)	(O4.5 V)	…	…
…	…	…	95	155	…	1920	O4:	Ca21	053840.949-690555.14	14.00	14.26	15.43	S	(0.21)	(O4 IIII)	…	…
…	…	…	84	145	…	1956:	O5:	Ca21	…	…	14.20	14.80	H	(0.21)	(O5 III)	…	…
…	…	…	92	…	…	…	O6 Vz	Be20	…	…	14.20	15.46	D	(0.21)	GHRS/G140L‡	4	…
…	…	1026	68	127	…	1787	O4–5 V	Be20	053843.180-690601.73	14.01	14.10	14.80	S	(0.21)	(O4.5 V)	…	…
…	…	1141	109	169	1035	2129	O8.5 I-II	He12	053844.312-690545.10	14.01	14.29	15.57	S	(0.21)	(O8.5 I)	…	…
…	…	970	83	142	1023	1580	O8 III-V	He12	053842.618-690610.00	14.02	14.22	15.31	S	(0.20)	(O8 III)	…	…
…	…	…	90	…	…	…	O4: V:	Be20	…	…	14.24	15.48	D	(0.20)	GHRS/G140L‡	4	…
…	…	…	…	141	373	2090	O9.5n	Wa14	053831.224-690553.03	…	14.24	15.27	S	(0.20)	(O9.5 III)	…	…
…	…	1191	…	128	575	2804	B0.7 III	Ev15	053844.904-690533.13	13.76	13.99	15.12	S	(0.20)	(B1 III)	…	…
…	…	…	88	165	1009	1732	O6.5 V–IIII	He12	053841.147-690602.91	14.07	14.23	15.42	S	(0.20)	(O6.5 III)	…	…
…	…	…	108	…	…	…	O7–8 V	Cr16	…	…	14.27	15.44	D	(0.20)	(O7 V)	…	…
…	…	729	138	144	…	1535	O5:	Ca21	053839.700-690608.63	14.08	14.20	15.31	S	(0.19)	(O5 III)	…	…
…	…	…	96	163	1008	1852	ON6.5 II–I	He12	053841.093-690558.40	14.09	14.32	…	S	(0.19)	(O6 I)	…	…
…	…	957	99	167	…	1527	O8 V	MH98	053842.445-690609.22	14.11	14.32	15.41	S	(0.19)	(O8 V)	…	…
…	…	1527	…	119	646	1951	B0.5 III(n)	Ev15	053850.263-690604.37	13.84	14.03	14.99	S	(0.19)	(B0 III)	…	…
…	…	…	93	…	…	…	O4–5 V	Cr16[a]	…	…	14.34	15.60	H	(0.18)	GHRS/G140L‡	4	…
…	…	531	…	166	…	1941	O8 V	Bo99	053836.728-690556.46	14.15	14.32	15.54	S	(0.18)	(O8 V)	…	…

Downloaded from https://academic.oup.com/mnras/article/527/3/9023/7455889 by guest on 16 February 2024

Table B1 – *continued*

R	Mk	P	HSH	SMB	VFTS	CCE	SpT	Ref	HTTP	m_{275W} mag	m_{F336W} mag	m_{F555W} mag	Ref	F_{1500} 10^{-13}	Spectrum (Template)	Ref	VMS
···	···	740	···	159	···	1537	O6:	Ca21	053839.837-690607.99	14.15	14.29	15.41	S	(0.18)	(O6 III)	···	···
···	···	···	94	···	···	···	O4–5 Vz	Be20	···	···	14.36	15.57	D	(0.18)	GHRS/G140L‡	4	···
···	···	1031	···	152	543	2521	O9 IV + O9.7: V	Wa14	053843.190-690527.52	14.17	14.26	15.44	S	(0.18)	(O9 V)	···	···
···	···	1288	···	175	597	375	O8–9 V(n)	Wa14	053846.063-690656.16	···	14.38	15.62	S	(0.18)	(O9 V)	···	···
···	···	1468	···	174	635	1334	O9.5 IV	Wa14	053849.039-690619.57	···	14.39	15.56	S	(0.18)	(O9 V)	···	···
···	···	···	101	178	1020	1401	O3–4	He12	053842.012-690616.83	14.21	14.40	15.53	S	(0.17)	(O3.5 V)	···	···
···	···	1145	···	168	561	2301	O9:(n)	Wa14	053844.368-690514.36	···	14.41	15.46	S	(0.17)	(O9 III)	···	···
···	···	901	···	138	518	1068	O3.5 III(f*)	Wa14	053841.934-690629.70	14.21	14.24	15.15	S	(0.17)	(O3 III)	···	···
···	···	887	85	154	1016	1371	O8 V	Bo99	053841.755-690619.06	14.22	14.33	15.31	S	(0.17)	(O8 V)	···	···
···	···	1336	···	176	···	2945	O8:	Ca21	053846.481-690542.20	14.22	14.39	15.54	S	(0.17)	(O8 III)	···	···
···	···	···	114	···	···	···	O5–6 V	Be20	···	···	14.43	15.68	D	(0.17)	(O5.5 V)	···	···
···	···	···	···	198	···	3167	O8:	Ca21	053841.818-690507.18	14.23	14.48	15.76	S	(0.17)	(O8 III)	···	···
···	···	841	98	157	···	2016	O4–6(n)(f)p	WB97	053841.186-690552.12	14.25	14.42	15.45	S	(0.17)	(O5 III)	···	···
···	···	···	100	···	···	···	B0 V	MH98	053842.206-690614.82	14.27	14.52	15.64	S,H	(0.17)	(B0 V)	···	···
···	···	992	···	182	···	2665	O7:	Ca21	053842.838-690530.36	14.29	14.44	15.56	S	(0.16)	(O7 III)	···	···
···	···	485	···	158	419	2897	O9: V(n)	Wa14	053835.906-690534.95	14.32	14.33	15.41	S	(0.16)	(O9 V)	···	···
···	···	···	113	190	···	1503	O9 V	MH98	053842.243-690612.23	14.32	14.53	15.62	S	(0.16)	(O9 V)	···	···
···	···	796	···	185	···	2565	O6:	Ca21	053840.665-690531.16	14.32	14.42	15.59	S	(0.16)	(O6 III)	···	···
···	···	670	···	172	456	2385	Onn(f)	Wa14	053838.818-690525.56	14.34	14.42	15.45	S	(0.15)	(O6 III)	···	···
···	···	994	···	146	···	2270	B0: V	Bo99	053842.841-690514.80	14.07	14.19	15.44	S	(0.15)	(B0 V)	···	···
···	···	1201	···	171	579	3116	O9:((n))	Wa14	053844.969-690507.65	14.36	14.56	15.47	S	(0.15)	(O9 V)	···	···
···	···	···	141	···	···	···	O5–6 V	Cr16	···	···	14.56	15.82	D	(0.15)	GHRS/G140L‡	4	···
···	···	···	116	···	···	···	O7 V	Be20	···	···	14.57	15.79	D	(0.15)	(O7 V)	···	···
···	···	···	115	···	···	···	O9 + V	Cr16	···	···	14.57	15.76	D	(0.15)	(O9 V)	···	···
···	···	1359	···	202	···	2782	O8:	Ca21	053846.901-690536.82	14.37	14.59	15.78	S	(0.15)	(O8 III)	···	···
···	···	1560	···	200	654	3010	O9 Vnn	Wa14	053851.159-690541.81	14.38	14.62	15.77	S	(0.15)	(O9 V)	···	···
···	···	···	···	179	570	3134	O9.5ne +	Wa14	053844.684-690545.19	14.39	14.42	···	S	(0.15)	(O9.5 III)	···	···
···	···	578	···	209	436	2223	O7–8 V	Wa14	053837.348-690521.29	14.39	14.58	15.93	S	(0.15)	(O7 V)	···	···
···	···	···	112	···	···	···	O7–9 Vz	Be20	···	···	14.61	15.74	D	(0.14)	GHRS/G140L‡	4	···
···	···	···	···	224	660	3027	O9.5 Vnn	Wa14	053851.812-690546.85	14.43	14.76	16.00	S	(0.14)	(O9 V)	···	···
···	···	···	132	···	···	···	O7: V	Be20	···	···	14.64	15.86	D	(0.14)	(O7 V)	···	···
···	···	348	···	227	400	2607	O9.7	Be20	053833..536-690521.73	14.45	14.79	16.05	S	(0.14)	(O9.5 III)	···	···
···	···	···	···	212	···	2776	O8:	Ca21	053843.127-690537.76	14.51	14.67	15.89	S	(0.13)	(O8 III)	···	···
···	···	490	···	140	422	1373	O4 III(f)	Wa14	053835.993-690616.91	14.15	14.23	15.15	S	0.13	COS/G140L	2	···
···	···	···	123	···	···	···	O6 V	Be20	053842.043-690604.58	14.52	14.71	15.76	S	(0.13)	(O6 V)	···	···
···	···	···	121	···	···	···	O9.5 V	Be20	···	···	14.73	15.85	D	(0.13)	(O9 V)	···	···
···	···	···	134	···	···	···	O7 Vz	Be20	053842.182-690604.95	14.52	14.74	15.44	S	(0.13)	(O7 V)	···	···
···	···	···	···	206	476	2789	O((n))	Wa14	053839.734-690539.27	14.53	14.73	15.72	S	(0.13)	(O6 III)	···	···
···	···	···	···	···	444	···	O9.7	Wa14	053838.011-690508.53	14.55	14.86	16.12	S	(0.13)	(B0 V)	···	···
···	···	···	···	218	615	1398	O9.5 IIInn	Wa14	053847.320-690617.74	···	14.78	15.64	S	(0.12)	(O9.5 III)	···	···
···	···	881	···	215	···	2389	O9:	Ca21	053841.643-690523.77	14.58	14.69	15.87	S	(0.12)	(O9 III)	···	···

Downloaded from https://academic.oup.com/mnras/article/527/3/9023/7455889 by guest on 16 February 2024

Table B1 – *continued*

R	Mk	P	HSH	SMB	VFTS	CCE	SpT	Ref	HTTP	m_{275W} mag	m_{F336W} mag	m_{F555W} mag	Ref	F_{1500} 10^{-13}	Spectrum (Template)	Ref	VMS
···	···	···	118	···	···	···	O7–8 V	Cr16	···	···	14.79	15.89	D	(0.12)	(O8 V)	···	···
···	···	···	···	211	···	1415	O7:	Ca21	053843.317-690611.65	14.61	14.80	15.92	S	(0.12)	(O7 III)	···	···
···	···	743	···	151	···	1523	O6:	Ca21	053839.846-690609.50	14.61	14.83	15.40	S	(0.12)	(O6 III)	···	···
···	···	918:	···	311:	···	1522	O7:	Ca21	053842.067-690608.95	···	14.82	15.81	S	(0.12)	(O7 III)	···	···
···	···	···	···	194	446	1339	Onn	Wa14	053838.245-690617.36	14.62	14.63	15.46	S	(0.12)	(O9.5 V)	···	···
···	···	915	144	238	···	2130	O8:	Ca21	053842.061-690552.23	14.62	14.85	15.97	S	(0.12)	(O8 III)	···	···
···	···	···	103	189	1010	1346	O7 V–III	Ma12	053841.255-690617.02	14.65	14.69	15.55	S	(0.11)	(O7 III)	···	···
···	···	···	···	226	382	2901	O4–5 V	Wa14	053832.253-690544.58	14.66	14.82	15.93	S	(0.11)	(O4.5 V)	···	···
···	···	···	140	187	1015	1734	O8: V	Le21	053841.637-690603.25	14.66	14.83	15.76	S	(0.11)	(O8 V)	···	···
···	···	···	···	208	443	1557	O7: V	Wa14	053837.972-690615.30	14.67	14.75	15.73	S	(0.11)	(O7 V)	···	···
···	···	547	···	214	432	466	O8–9 V	Wa14	053837.030-690650.70	···	14.88	15.73	S	(0.11)	(O8 V)	···	···
···	···	1369	···	219	613	2005	O8.5 Vz	Wa14	053847.161-690554.46	14.68	14.80	15.80	S	(0.11)	(O8 V)	···	···
···	···	853	···	177	1011	1447	O5 V	Le21	053841.348-690614.04	14.70	14.75	15.39	S	(0.11)	(O4.5 V)	···	···
···	···	···	126	193	1004	1725	O9.5 V-III	He12	053840.831-690604.60	14.70	14.82	15.59	S	(0.11)	(O9.5 III)	···	···
···	···	803	···	213	491	276	O6 V	Wa14	053840.846-690657.51	···	14.96	15.69	S	(0.10)	(O6 V)	···	···
···	···	···	···	239	649	2038	O9.5 V	Wa14	053850.610-690554.57	14.77	15.02	16.14	S	(0.10)	(O9 V)	···	···
···	···	1224	···	231	···	1472	O6:	Ca21	053845.213-690613.62	14.78	14.90	15.99	S	(0.10)	(O6 III)	···	···
···	···	···	···	277	···	2453	O8:	Ca21	053840.166-690520.63	14.78	15.04	16.34	S	(0.10)	(O8 III)	···	···
···	···	1401	···	234	619	689	O7–8 V(n)	Wa14	053847.717-690644.94	···	14.99	16.07	S	(0.10)	(O8 V)	···	···
···	···	···	102	207	···	···	O2–3 III	Cr16	053843.165-690600.85	14.79	14.79	15.52	S	(0.10)	(O2.5 III)	···	···
···	···	1087	···	272	···	1275	O8:	Ca21	053843.749-690621.89	14.79	15.06	16.27	S	(0.10)	(O8 III)	···	···
···	···	1086	···	247	···	2454	O7:	Ca21	053843.709-690521.64	14.80	14.97	16.16	S	(0.10)	(O7 III)	···	···
···	···	982	160	258	···	2044	O4: V	Pa93	053842.721-690552.80	14.80	14.98	16.14	S	(0.10)	(O4 V)	···	···

Sp Types: Be20: Bestenlehner et al. (2020); Be22: Bestenlehner et al. (2022); Bo99: Bosch et al. (1999); Ca21 Castro et al. (2021b); Cr10: Crowther et al. (2010); Cr16: Crowther et al. (2016); Cr22: Crowther et al. (2022); CD98: Crowther & Dessart (1998); CS97: Crowther & Smith (1997); CW11: Crowther & Walborn (2011); De97: de Koter, Heap & Hubeny (1997); Do13:Doran et al. (2013) Ev11: Evans et al. (2011); Ev15: Evans et al. (2015); He12: Hénault-Brunet et al. (2012); Ka22 Kalari et al. (2022); Le21 : D. Lennon (priv comm, 2021); Ma02: Massey, Penny & Vukovich (2002); Ma05: Massey et al. (2005); Ma12: Massey et al. (2012); MH98 : Massey & Hunter (1998); Pa93: Parker (1993); Te19: Tehrani et al. (2019); Wa14: Walborn et al. (2014); WB97: Walborn & Blades (1997)

Spectroscopy: 1. GO 16272 (Shenar); 2. GO 15629 (Mahy); 3. Roman-Duval et al. (2020); 4. Heap, Ebbets & Malumuth (1992); 5. de Koter, Heap & Hubeny (1998); 6. Massey et al. (2005). Note: (a) spectral type of HSH 119 (fainter component of blend with m_{F336W} = 15.0 mag)

Photometry: D: De Marchi et al. (2011); H: Hunter et al. (1995); S: Sabbi et al. (2016)

Downloaded from https://academic.oup.com/mnras/article/527/3/9023/7455889 by guest on 16 February 2024

Table B2. Stars within the *IUE* 3 × 3 arcmin^2 Vacca et al. (1995) field of view that are exterior to MUSE, sorted by far-UV flux (F_{1500} units of erg s^{-1} cm^{-2} Å^{-1}), measured from *IUE*/SWP spectroscopy or estimated from photometry, the latter indicated in parentheses. See Table B1 for references in common.

R	Mk	P	HSH	SMB	VFTS	CCE	SpT	Ref	HTTP	m_{275W} mag	m_{F336W} mag	m_{F555W} mag	Ref	F_{1500} 10^{-13}	Spectrum (Template)	Ref	VMS
139	···	952	···	2	527	···	O6.5 Iafc + O7 Iaf	Wa14	053842.351-690458.19	10.97	10.86	12.02	S	6.21	(O7 I)	1	···
145	···	1788	···	···	695	···	WN6h + O3/5 If/WN7	Sh17	053857.072-690605.58	···	10.88	11.94	S	4.21	(WN6)	1	✓
135	···	355	···	12	402	···	WN5: + WN7	Sh19	053833.615-690450.47	11.63	11.68	12.82	S	2.34	(WN6)	1	···
···	23	1163	···	42	566	···	O3 III(f*)	Wa14	053844.558-690451.19	12.40	12.68	14.03	S	(0.91)	(O3 III)	···	···
···	···	1035	···	···	···	···	O3–6 V	WB97	053843.159-690441.82	12.93	13.35	14.75	S	(0.56)	(O4.5 V)	···	···
···	57	541	···	79	429	···	O7: V + B1: V	Sh22	053836.854-690458.28	12.95	13.32	14.70	S	(0.55)	(O7 V)	···	···
···	···	809	···	133	···	···	O8–9 V	Bo99	053840.773-690452.83	13.67	14.01	15.34	S	(0.28)	(O9 V)	···	···
···	···	1077	···	···	550	···	O5 V((f))z	Wa14	053843.599-690442.44	13.78	14.12	15.42	S	(0.26)	(O5 V)	···	···
···	···	124	···	···	350	···	O8.5 V + O9.5 V	Sh22	053828.057-690629.05	13.79	14.09	15.03	S	(0.25)	(O9 V)	···	···
···	···	83	···	···	339	···	O9.5 IV	Wa14	053826.218-690501.84	13.83	14.15	15.52	S	(0.24)	(O9 V)	···	···
···	···	169	···	107	360	···	O9.7	Wa14	053829.421-690521.20	13.84	13.85	14.85	S	(0.24)	(O9.5 III)	···	···
···	···	466	···	150	415	···	O9.5 V	Wa14	053835.480-690457.67	13.90	14.17	15.50	S	(0.23)	(O9 V)	···	···
···	60	195	···	98	363	···	B0.2 III-II	Ev15	053829.986-690505.18	13.61	13.68	14.86	S	(0.23)	(B0 III)	···	···
···	···	1052	···	···	546	···	O8–9 III	Wa14	053843.373-690446.34	14.02	14.21	15.41	S	(0.20)	(O8 III)	·	···
···	···	1729	···	···	686	···	B0.7 III	Ev15	053855.634-690723.71	14.05	14.15	15.05	S	(0.15)	(B1 III)	···	···
···	···	1756	···	···	688	···	O9.7 III	Wa14	053856.058-690554.04	14.45	14.70	15.64	S	(0.14)	(O9.5 III)	···	···
···	···	955	···	···	529	···	O9.5(n)	Wa14	053842.374-690443.12	14.55	14.89	16.09	S	(0.13)	(O9.5 III)	···	···
···	···	905	···	···	521	···	O9 V(n)	Wa14	053841.955-690704.97	···	14.82	15.90	S	(0.12)	(O9 V)	···	···
···	···	171	···	216	361	···	O8.5 V	Wa14	053829.482-690620.55	14.63	14.81	15.75	S	(0.12)	(O8 V)	···	···
···	···	1840	···	···	707	···	B0.5 V	Ev15	053858.907-690642.05	···	14.55	15.65	S	(0.12)	(B0.5 V)	···	···
···	···	···	···	···	486	···	B1-2ne +	Ev15	053840.604-690456.02	14.20	14.16	15.28	S	(0.11)	(B1 III)	···	···
···	···	···	···	319	412	···	O9.7	Wa14	053834.901-690453.74	14.71	15.14	16.47	S	(0.11)	(O9.5 III)	···	···
···	···	1209	···	205	···	···	O9–B0 V	Bo99	053845.055-690446.88	14.74	14.85	15.67	S	(0.11)	(O9 V)	···	···
···	···	1429	···	···	621	···	O2 V((f))z	Wa14	053848.089-690442.18	14.80	14.86	15.59	S	(0.10)	(O2 V)	···	···

Sp Types: Sh17: Shenar et al. (2017); Sh19: Shenar et al. (2019); Sh22: Shenar et al. (2022)
Spectroscopy: 1. Fitzpatrick & Savage (1984)

Downloaded from https://academic.oup.com/mnras/article/527/3/9023/7455889 by guest on 16 February 2024

APPENDIX C: FAR-UV CALIBRATIONS

We calibrate F_{1500} fluxes against $m_{\rm F275W}$ or $F_{\rm F336W}$ photometry using reference O stars in 30 Doradus that have been observed in the far-UV. These are listed in Table C1, sorted by F_{1500} with references to spectral types, photometry and HST data sets identical to Table B1. Column densities, $\log N$(H I) from fits to Lyα are included and should be reliable to ±0.05 dex (e.g. Welty, Xue & Wong (2012) obtain $\log N({\rm H\,I/cm^2}) = 21.79$ for Mk 42). Comparisons are presented in Fig. 3, with calibrations presented in Equations 1 and 2. Since we utilize templates spanning a range of extinctions, we also adjust far-UV slopes (λλ1160-1700) of templates to individual O stars within the MUSE field from their $_{\rm F336W}$ − $m_{\rm F555W}$ colours. These are presented in Fig. C1 with the fit obtained as follows

$$F_{1700}/F_{1160} \simeq 1.76(m_{\rm F336W} - m_{\rm F555W}) + 3.33. \quad \text{(C1)}$$

30 Doradus O stars external to the MUSE field reveal a somewhat different behaviour, likely as a result of lower dust extinction.

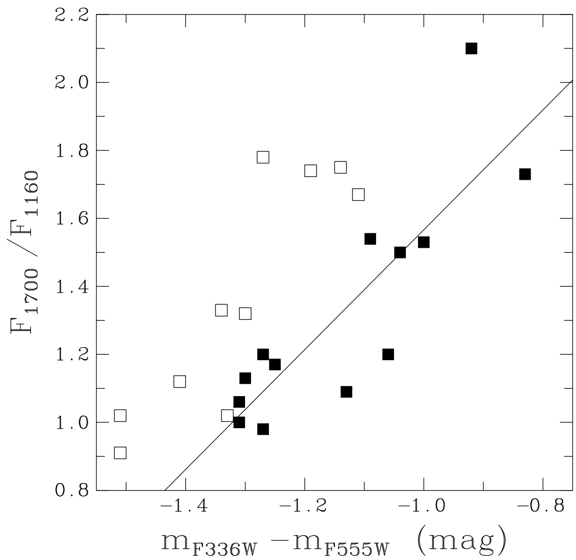

Figure C1. Relationship between ($m_{\rm F336W}$ − $m_{\rm F555W}$) colour and far-UV slope, F_{1700}/F_{1160}, for O stars in 30 Doradus (solid within MUSE field) with far-UV spectroscopy and HST/WFC3 photometry. The solid line is a linear fit to observations within the MUSE field.

Downloaded from https://academic.oup.com/mnras/article/527/3/9023/7455889 by guest on 16 February 2024

Table C1. Reference O stars within 30 Doradus used to calibrate far-UV fluxes (units are erg s^{-1} cm^{-2} $Å^{-1}$), $\lambda\lambda$1160-1700 slopes and log N(H I) from fits to Lyα. Sources within MUSE footprint are indicated. References are as for Table B1.

Star	Sp Type	Ref	m_{F275W} (mag)	m_{F336W} (mag)	m_{F555W} (mag)	Ref	F_{1500} 10^{-13}	F_{1700}/F_{1160}	log N(H I) cm^{-2}	HST data set	Ref	MUSE
Mk 42	O2 If	CW11	11.08	11.51	12.82	S	3.01	1.00	21.75	STIS/E140M	3	✓
Mk 39	O2.5 If/WN6 +	Cr22	11.38	11.66	12.95	S	2.74	1.13	21.75	COS/G130M + G160M	3	✓
VFTS 506	ON2 V	Wa14	11.74	12.01	13.32	S	2.04	1.06	21.8	COS/G130M + G160M	3	✓
Mk 30	O2 If/WN5	CW11	11.91	12.22	13.48	S	1.85	0.98	21.75	COS/G130M + G160M	3	✓
VFTS 180	O3 If*	Wa14	...	12.11	13.52	S	1.57	1.12	21.6	COS/G130M + G160M	3	···
VFTS 87	O9.7 Ib-II	Wa14	11.97	12.09	13.60	S	1.52	1.02	21.6	STIS/E140M	3	···
VFTS 267	O3 III-I	Wa14	···	12.15	13.49	S	1.39	1.33	21.75	COS/G130M + G160M	3	···
VFTS 440	O6–6.5 III	Wa14	12.15	12.44	13.69	S	0.96	1.17	21.75	STIS/E140M	2	✓
Mk 37a	O3.5 If/WN7	CW11	12.33	12.48	13.52	S	0.82	1.50	···	STIS/G140L	6	✓
Mk 33S	O3 III	Ma15	12.48	12.76	13.81	S	0.79	1.20	···	STIS/G140L	6	✓
VFTS 586	O4 Vz	Wa14	13.06	13.50	15.02	S	0.76	0.91	21.75	COS/G130M + G160M	3	···
VFTS 352	O4.5 Vz + O5.5 Vz	Wa14	12.75	13.13	14.46	S	0.70	1.02	21.8	COS/G130M + G160M	3	···
Mk 55	O6 Vnn	Wa14	12.79	13.04	14.34	S	0.61	1.32	21.75	COS/G130M + G160M	3	···
VFTS 385	O4–5 V	Wa14	13.22	13.38	14.65	S	0.51	1.20	21.8:	COS/G140L	2	✓
VFTS 404	O3.5 V	Wa14	12.76	12.95	14.13	S	0.49	1.74	21.9	COS/G130M + G160M	3	···
Mk 51	O3.5 If/WN7	CW11	···	12.98	13.81	S	0.45	1.73	21.9:	COS/G140L	2	✓
Mk14S	O4 III	Wa14	13.01	13.19	14.29	S	0.43	1.54	21.9:	COS/G140L	2	✓
Mk 4	O7 II	Wa14	···	13.37	14.38	S	0.41	1.53	22.0:	COS/G140L	2	✓
VFTS 667	O6 V	Wa14	···	13.95	15.08	S	0.33	1.09	21.9:	COS/G140L	2	✓
VFTS 169	O2.5 V	Wa14	13.64	13.46	14.60	S	0.32	1.75	22.0	COS/G130M + G160M	3	···
VFTS 190	O7 Vnnp	Wa14	13.70	13.43	14.70	S	0.28	1.78	21.7	COS/G130M + G160M	3	···
VFTS 66	O9.5 III	Wa14	14.40	14.49	15.61	S	0.14	1.67	22.0	COS/G130M + G160M	3	···
VFTS 422	O4III(f)	Wa14	14.15	14.23	15.15	S	0.13	2.10	21.9:	COS/G140L	2	✓

This paper has been typeset from a TEX/LATEX file prepared by the author.

Downloaded from https://academic.oup.com/mnras/article/527/3/9023/7455889 by guest on 16 February 2024

© 2023 The Author(s).
Published by Oxford University Press on behalf of Royal Astronomical Society. This is an Open Access article distributed under the terms of the Creative Commons Attribution License (http://creativecommons.org/licenses/by/4.0/), which permits unrestricted reuse, distribution, and reproduction in any medium, provided the original work is properly cited.